Metadata of the article that will be visualized in OnlineFirst

ArticleTitle	A closed-form yield criterion to porous materials with Mises–Schleicher–Burzyński matrix containing cylindrical voids
Article Sub-Title	
Article CopyRight	The Author(s), under exclusive licence to Springer-Verlag GmbH, AT part of Springer Nature (This will be the copyright line in the final PDF)
Journal Name	Acta Mechanica

Corresponding Author	Family Name	**Santos**
	Particle	
	Given Name	**Tiago dos**
	Suffix	
	Division	Departamento de Engenharia Mecânica
	Organization	Universidade Federal de Santa Maria
	Address	Av. Roraima, 1000, Prédio 7, Santa Maria, RS, 97105-900, Brazil
	Phone	
	Fax	
	Email	tsantos.dem@smail.ufsm.br
	URL	
	ORCID	http://orcid.org/0000-0002-5168-7282
Author	Family Name	**Vadillo**
	Particle	
	Given Name	**Guadalupe**
	Suffix	
	Division	Department of Continuum Mechanics and Structural Analysis
	Organization	University Carlos III of Madrid
	Address	Avda. de la Universidad, 30, 28911, Leganés, Madrid, Spain
	Phone	
	Fax	
	Email	gvadillo@ing.uc3m.es
	URL	
	ORCID	

	Received	17 July 2020
Schedule	Revised	6 December 2020
	Accepted	16 December 2020

Abstract

This work develops a closed-form yield criterion applicable to porous materials with pressure-dependent matrix presenting tension–compression asymmetry (Mises–Schleicher–Burzyński material) containing parallel cylindrical voids. To develop the strength criterion, the stress-based variational homogenization approach due to Cheng et al. (Int J Plast 55:133–151, 2014) is extended to the case of a hollow cylinder under generalized plane strain conditions subjected to axisymmetric loading. Adopting a strictly statically admissible trial stress field, the homogenization procedure results in an approximate yield locus depending on the current material porosity, tension–compression material asymmetry, the mean lateral stress and an equivalent shear stresses. The analytical criterion provides exact solutions for purely hydrostatic loading. Theoretical results are compared with finite element (FE) simulations considering cylindrical unit-cells with distinct porosity levels, different values of the tension–compression asymmetry and a wide range of stress triaxialities. Based on comparisons, the theoretical results are found to be in good agreement with FE simulations for most of the loading conditions and material features considered in this study. More accurate theoretical predictions are provided when higher material porosities and/or lower tension–compression asymmetries are considered. Overall, the main outcome of this work is a closed-form yield function proving fairly accurate predictions to engineering applications, in which pressure-dependent and tension–compression asymmetric porous materials with cylindrical voids are dealt with. This can be the case of honeycomb structures or additively manufactured materials, in which metal matrix composites are employed.

Footnote Information

Acta Mech
https://doi.org/10.1007/s00707-020-02925-y

ORIGINAL PAPER

Tiago dos Santos · Guadalupe Vadillo

A closed-form yield criterion to porous materials with Mises–Schleicher–Burzyński matrix containing cylindrical voids

Received: 17 July 2020 / Revised: 6 December 2020 / Accepted: 16 December 2020

Abstract This work develops a closed-form yield criterion applicable to porous materials with pressure-dependent matrix presenting tension–compression asymmetry (Mises–Schleicher–Burzyński material) containing parallel cylindrical voids. To develop the strength criterion, the stress-based variational homogenization approach due to Cheng et al. (Int J Plast 55:133–151, 2014) is extended to the case of a hollow cylinder under generalized plane strain conditions subjected to axisymmetric loading. Adopting a strictly statically admissible trial stress field, the homogenization procedure results in an approximate yield locus depending on the current material porosity, tension–compression material asymmetry, the mean lateral stress and an equivalent shear stresses. The analytical criterion provides exact solutions for purely hydrostatic loading. Theoretical results are compared with finite element (FE) simulations considering cylindrical unit-cells with distinct porosity levels, different values of the tension–compression asymmetry and a wide range of stress triaxialities. Based on comparisons, the theoretical results are found to be in good agreement with FE simulations for most of the loading conditions and material features considered in this study. More accurate theoretical predictions are provided when higher material porosities and/or lower tension–compression asymmetries are considered. Overall, the main outcome of this work is a closed-form yield function proving fairly accurate predictions to engineering applications, in which pressure-dependent and tension–compression asymmetric porous materials with cylindrical voids are dealt with. This can be the case of honeycomb structures or additively manufactured materials, in which metal matrix composites are employed.

1 Introduction

Porous materials are known to be present in many engineering applications and the porosity is known to influence the mechanical behavior of such materials. For example, material porosity has been reported to be intimately related to the ductile fracture and failure of metallic materials [2]. In addition, when it comes to geophysics and civil engineering, material porosity is thought to be an intrinsic feature of soils, rocks, concrete and asphalt that significantly influences their overall mechanical behavior, regarding, e.g., stability and fracture strength [9, 10]. 1

The constitutive modelling of the mechanical behavior of porous metallic materials may be traced back to the pioneering works of McClintock [26], Rice and Tracey [35] and Gurson [17]. The analyses due to McClintock

T. dos Santos (✉)
Departamento de Engenharia Mecânica, Universidade Federal de Santa Maria, Av. Roraima, 1000, Prédio 7, Santa Maria, RS 97105-900, Brazil
e-mail: tsantos.dem@smail.ufsm.br

G. Vadillo
Department of Continuum Mechanics and Structural Analysis, University Carlos III of Madrid, Avda. de la Universidad, 30, 28911 Leganés, Madrid, Spain
e-mail: gvadillo@ing.uc3m.es

[26] and Rice and Tracey [35], on the growth of voids in ductile matrix materials, have provided the basis for the subsequent study of Gurson [17], who proposed a macroscopic yield criterion for porous media with a von Mises matrix material containing either cylindrical or spherical voids. Gurson's development consists of a kinematic limit analysis, which provided yield criteria to porous plastic solids explicitly accounting for the porosity influence on the overall material strength. Later, Gurson's approach has been heuristically extended by Tvergaard [49] and Tvergaard and Needleman [50] in an effort to provide a better agreement when compared to unit-cell simulations. Therefore, resulting in the well-known GTN model that has been widely employed within modelling frameworks addressing ductile damage, fracture and failure in incompressible matrix materials (see for instance the review of Benzerga and Leblond [2]).

Many researches have lead to more general approaches, where Gursons's model has been extended in an effort to incorporate pore shape and/or the effect of matrix anisotropy (see Monchiet et al. [28]; Cazacu and Stewart [6]; Keralavarma and Benzerga [21]; Monchiet et al. [29]; Keralavarma and Benzerga [22], to cite few works). Regarding both tension–compression asymmetry and plastic anisotropy, Cazacu and Stewart [6] have developed an analytic plastic potential for a void-matrix aggregate with a random distribution of spherical voids. They have employed an upper bound approach for a matrix material obeying the yield criterion developed by Cazacu et al. [5], which can describe both the anisotropy and the tension–compression asymmetry of the matrix. Monchiet et al. [28] investigated the combined effects of both void shape and matrix anisotropy on the macroscopic response of ductile porous solids. They have extended the analysis due to Gologanu et al. [15] to the case of an anisotropic matrix obeying the criterion of Hill [20]. Keralavarma and Benzerga [21] have considered a class of anisotropic porous media with spheroidal voids arbitrarily oriented in an orthotropic matrix. Their model has been numerically assessed in a subsequent work [22], where theoretical predictions have been compared with rigorous upper bounds obtained from numerical analysis of spheroidal unit-cells. Moreover, Monchiet et al. [29], employing Eshelby-like velocity fields, also provided a closed-form anisotropic yield criterion for a rigid ideal-plastic von Mises matrix containing spheroidal cavities.

While all works cited above have addressed only pressure-independent matrix materials, proposals dealing with pressure-dependent ones have also been proposed. In this sense, studies have been devoted to extend Gurson's approach to porous solids with either Drucker–Prager [16, 42, 44]—that has a linear pressure-dependence—or Green [14, 40] matrix materials—having a symmetric parabolic pressure-dependence. See the reviews of Dormieux et al. [11], Shen and Shao [38] and Shen et al. [42] for more detailed discussions.

While approaches considering porous media having either Drucker–Prager or Green matrices have provided suitable results to rock-like and powder materials, they have not been adequate to model the behavior of porous solids with non-linearly pressure-dependent matrix presenting strong tension–compression asymmetry, such as some polymers and metal matrix composites [3, 24, 36, 54]. In the case of metal matrix composites, possible causes for the tension–compression asymmetry are reported to be related to the residual stresses due to the thermal expansion mismatch between matrix and reinforcements (see for instance Zhang et al. [54]). The yield behavior of such materials is better represented by parabolic type pressure-dependent yield criteria that accounts for tension–compression asymmetry, such as the Mises–Schleicher [36] or Burzyński [3] ones.

In the context of pressure-dependent and tension–compression asymmetric porous materials, Lee and Oung [24] have employed Gurson's approach to obtain closed-form yield criteria to porous solids with a Mises–Schleicher matrix having either spherical or cylindrical voids. However, the obtained criteria were not suitable to high-stress triaxiliaties and did not recover Gurson's model for the particular case of a von Mises matrix. Thus, the model was empirically modified by the authors in order to comply with the last feature. Furthermore, employing a simple static procedure, Durban et al. [12] derived closed form yield functions for spherically voided solids with pressure-sensitive matrix considering either Drucker–Prager or Mises–Schleicher matrix materials. Subsequently, Monchiet and Kondo [30] have developed an exact solution for porous materials with Mises–Schleicher matrix, considering the problem of a hollow sphere subjected to purely hydrostatic load on its external boundary.

Results due to Monchiet and Kondo [30] for spherical voids have been considered in further numerical limit analysis on spherical cells with Mises–Schleicher matrix material [33, 34], providing both upper and lower bounds to the macroscopic yield criteria. Shen et al. [41], employing the exact solution of Monchiet and Kondo [30], have proposed a new macroscopic criterion to porous materials with Mises–Schleicher matrix. The new macroscopic yield function has been compared with the theoretical approaches due to Lee and Oung [24] and to Durban et al. [12], and also with the numerical bounds obtained by Pastor et al. [34]. The model developed by Shen et al. [41] presented a better agreement with numerical simulations. This model was subsequently employed to describe the mechanical behavior of rock-like porous materials [19, 39].

Shen et al. [43] have improved the criterion of Shen et al. [41] in an effort to provide better predictions for pure deviatoric stress states. The authors (Shen et al. [43]) have employed the variational stress-based homogenization approach proposed by Cheng et al. [8], in which statically admissible microscopic trial stress fields have to be constructed (see also Yi and Duo [53]). To build the trial stress fields, Shen et al. [43] have adopted the exact solution of Monchiet and Kondo [30], for purely hydrostatic stresses, and that employed by Zhang et al. [55], for a pure deviatoric loading, which has been based on the Boussinesq–Papkovich–Neuber solution.

A large improvement of the early work of Lee and Oung [24] has been recently achieved in the works of Monchiet and Kondo [30]; Pastor et al. [34]; Shen et al. [41] and Shen et al. [43] regarding porous solids with Mises–Schleicher matrix materials. However, except for the work of Lee and Oung [24], other proposals cited above have considered only spherical voids in their developments. To the best of our knowledge, except for Lee and Oung [24], a strength criterion to porous materials with Mises–Schleicher matrix containing cylindrical voids has not been proposed in the open literature. Nevertheless, the study of porous material with cylindrical voids/cavities has also a significant importance in engineering applications, such as thick-walled honeycomb structures and additively manufactured lightweight materials in aerospace industry [45]. Particularly, the additive manufacturing process has provided new geometric freedom for metal matrix composites to be used in lightweight structures [25].

Aiming at addressing the yield behavior of pressure-dependent and tension–compression asymmetric porous materials, this work develops an approximate strength criterion to porous solids with a Mises–Schleicher–Burzyński matrix material containing cylindrical voids. With this goal, the variational stress-based homogenization of Cheng et al. [8] is then employed. In this approach, a trial stress field satisfying the equilibrium equations is then built-up. In addition, the yield condition is relaxed by means of a Lagrange multiplier, being satisfied only in an average way. According to the literature, this kind of approach is known to provide quasi lower bounds [8].

In this work, following the procedure outlined by Shen et al. [43], the microscopic trial stress field results from the superposition of two stress tensors. In the first case, the exact solution developed by Monchiet and Kondo [30], considering a hollow sphere, is extended to the case of a hollow cylinder subjected to tractions on its external boundary (see Appendix A). External loads consists of longitudinal stresses applied on the top and bottom surfaces and also to radial stress applied at the outer radius. A specific feature of the first microscopic trial stress field is that the longitudinal stress is assumed to be equal to the hydrostatic stress. As it will be shown throughout the work, this hypothesis results in a purely hydrostatic macroscopic stress field. The second microscopic trial stress state is obtained from a simple homogeneous longitudinal loading applied on both top and bottom surfaces (see Appendix B). To be highlighted that in this work the microscopic trial stress field comply with stress-free boundary conditions at the cavity wall. This was not the case in the original approach due to Cheng et al. [8], where a hollow sphere was considered.

This work is organized as follows. Section 3 describes the stress-based variational homogenization approach of Cheng et al. [8] and Shen et al. [37] to be applied to the case of a hollow cylinder. The finite element model employed in this work is described in Sect. 4. In Sect. 5, the results obtained using the developed macroscopic yield criterion are presented and discussed. The theoretical results are compared with other models to porous materials with cylindrical voids [17, 24]—see Appendix D—and also with finite element results. The final conclusions and remarks are given in Sect. 6.

2 Constitutive framework

This section briefly outlines the main features of the constitutive model studied in this work. The matrix material is considered to present a pressure-dependent plastic behavior with tension–compression asymmetry. Therefore, its plastic behavior is assumed to follow the Mises–Schleicher [36] yield function:

$$\phi = \sigma_e^2 + 3(k-1)\sigma_h\sigma_T - (\sigma_T)^2 k \leq 0 \tag{1}$$

where $\sigma_e = \sqrt{\frac{3}{2}\boldsymbol{s} : \boldsymbol{s}}$ is the von Mises equivalent stress, $\sigma_h = \frac{1}{3}\boldsymbol{\sigma} : \mathbf{1}$ is the hydrostatic stress, being $\mathbf{1}$ the second-order unity tensor and $\boldsymbol{s} = \boldsymbol{\sigma} - \sigma_h \mathbf{1}$ the deviatoric part of the Cauchy stress tensor $\boldsymbol{\sigma}$. Moreover, in Eq. (1), $k = \sigma_C/\sigma_T$ is the ratio between the yield stresses in compression, σ_C, and tension, σ_T. Notice that, if the following constants are defined,

$$\alpha = \frac{(k-1)}{\sqrt{k}} \quad \text{and} \quad \sigma_0 = \sqrt{k}\sigma_T \tag{2}$$

the form employed by Monchiet and Kondo [30] is obtained:

$$\phi = \sigma_e^2 + 3\alpha\sigma_0\sigma_h - \sigma_0^2 \leq 0 \tag{3}$$

In this work, the material is considered to be perfectly plastic. Therefore, the yield stresses, σ_C and σ_T, are constant. The yield function provided in Eq. (3) can be seen as a particular case of Burzyński's model [3, 52]. Therefore, we will call it Mises–Schleicher–Burzyński criterion.

Furthermore, the material is assumed to present an elastoplastic behavior. Thus, the deformation rate tensor is taken to be the sum of an elastic $\boldsymbol{d}^e$ and a plastic $\boldsymbol{d}^p$ part:

$$\boldsymbol{d} = \boldsymbol{d}^e + \boldsymbol{d}^p \tag{4}$$

The elastic part relates to the rate of the stress by means of a hypo-elastic law:

$$\overset{\triangledown}{\boldsymbol{\sigma}} = \boldsymbol{C} : \boldsymbol{d}^e = \boldsymbol{C} : (\boldsymbol{d} - \boldsymbol{d}^p) \tag{5}$$

where $\overset{\triangledown}{\boldsymbol{\sigma}}$ is the Jaumann stress rate and $\boldsymbol{C}$ is the fourth-order tensor of isotropic elastic moduli:

$$\boldsymbol{C} = \frac{E}{1+\nu}\boldsymbol{I}' + \frac{E}{3(1-2\nu)}\boldsymbol{1} \otimes \boldsymbol{1} \tag{6}$$

in which E is the Young's modulus, ν is the Poisson's ratio, $\boldsymbol{1}$ is the unit second-order tensor, and $\boldsymbol{I}'$ is the unit deviatoric fourth-order tensor.

The plastic deformation rate tensor is assumed to follow an associative flow rule:

$$\boldsymbol{d}^p = \dot{\lambda}\frac{\partial\phi}{\partial\boldsymbol{\sigma}} \tag{7}$$

where $\dot{\lambda}$ is a non-negative plastic multiplier obeying the dissipation consistency:

$$\dot{\lambda} = \frac{\sigma_T \dot{\bar{\varepsilon}}^p}{\boldsymbol{\sigma} : \frac{\partial\phi}{\partial\boldsymbol{\sigma}}} \tag{8}$$

where $\dot{\bar{\varepsilon}}^p$ is the effective strain rate (see e.g. Vadillo et al. [52]). Moreover, the constitutive model follows both the Kuhn-Tucker loading-unloading, $\dot{\lambda} \geq 0$, $\phi \leq 0$, $\dot{\lambda}\phi = 0$, and the consistency, $\dot{\lambda}\dot{\phi} = 0$, conditions.

3 Stress-based variational homogenization

This section briefly outlines the main features of the stress-based variational homogenization approach. For a detailed description, the reader is referred to the works of Cheng et al. [8], Shen et al. [37] and Shen et al. [43].

Let us consider a material containing periodically distributed parallel cylindrical voids, as shown in Fig. 1a. Due to material periodic pattern, the homogenization process is carried out considering the unit cylindrical cell Ω shown in Fig. 1b. The unit-cell is composed of void ω and matrix Ω_m domains, such that $\Omega = \Omega_m \cup \omega$. The macro-element Ω is bounded by surface $\partial\Omega$ and the void ω by $\partial\omega$. The initial height of the cell is H_0, the initial inner and outer radii are a_0 and b_0, respectively (see Fig. 1b). The stress-based homogenization approach assumes an axisymmetric model subjected to radial Σ_r and longitudinal Σ_z macroscopic stresses on its outer surface, while void surface is stress-free, as illustrated in Fig. 1c. Therefore, deformation occurs in a manner that both the cell and the void remain cylindrical during the whole process. Matrix material is assumed to obey the constitutive model provided in Sect. 2. However, it is assumed to present a rigid-plastic behavior: $\boldsymbol{d} = \boldsymbol{d}^p$ (see Eq. (4)).

Considering a generalized plane strain and cylindrically symmetric problem, with cylindrical coordinates (r, θ, z), it is assumed that the circumferential displacement u_θ is null, the radial displacement u_r varies only with the radial coordinate r. Moreover, the longitudinal displacement u_z, in addition to be constant in plane (r, θ), is assumed to vary linearly with the longitudinal axis z, providing a uniform longitudinal strain ε_z.

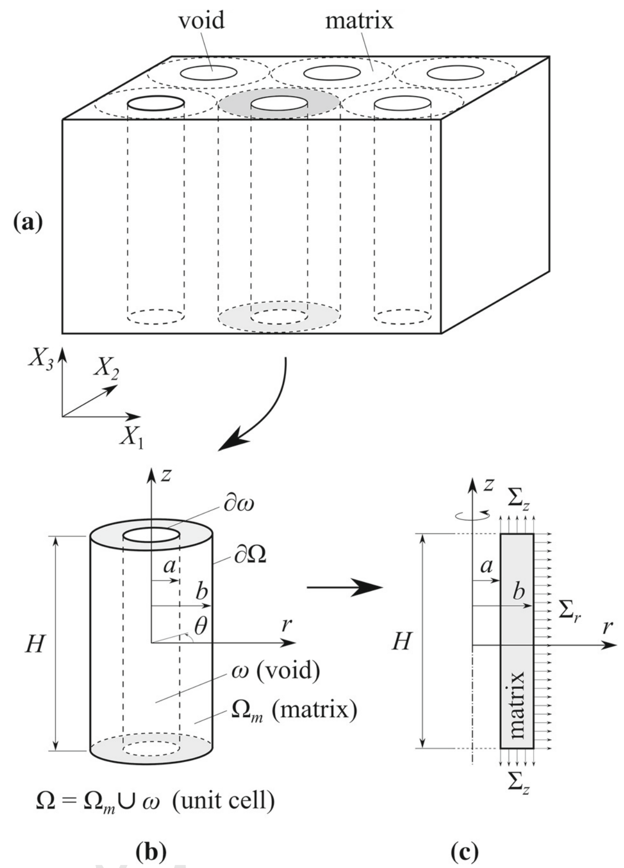

Fig. 1 **a** Schematic representation of the porous material containing distributed parallel cylindrical voids. **b** Unit cylindrical cell, Ω, composed of void ω and matrix Ω_m domains, where geometric parameters are illustrated. **c** Axisymmetric model subjected to radial Σ_r and longitudinal Σ_z macroscopic stresses on its outer surface, while void surface is stress-free

Regarding the stress field, it is assumed that all shear stresses are null, both radial σ_r and circumferential σ_θ stresses depend only on the radial coordinate r, and the longitudinal stress σ_z is uniform. Therefore, disregarding body forces and inertia effects, the equilibrium equation reads:

$$\frac{d\sigma_r}{\mathrm{d}r} + \frac{\sigma_r - \sigma_\theta}{r} = 0 \tag{9}$$

Since the radial displacement $u(r)$ is the only non-vanishing in-plane displacement, the active strain rates $(\dot{\varepsilon}_r, \dot{\varepsilon}_\theta, \dot{\varepsilon}_z)$ are then given by:

$$\dot{\varepsilon}_r = \frac{d\dot{u}}{\mathrm{d}r}, \quad \dot{\varepsilon}_\theta = \frac{\dot{u}}{r}, \quad \dot{\varepsilon}_z = \dot{E}_3 \tag{10}$$

being $\dot{E}_3 = \dot{H}/H$ the rate of macroscopic logarithmic principal strain in X_3 direction (axes X_3 and z are parallel, see Fig. 1).

Both the macroscopic stress $\boldsymbol{\Sigma}$ and the macroscopic deformation rate $\boldsymbol{D}$ are obtained from volume averages of their microscopic counterparts $\boldsymbol{\sigma}$ and $\boldsymbol{d}$ (see for instance Suquet [47]):

$$\boldsymbol{\Sigma} = \frac{1}{|\Omega|}\int_\Omega \boldsymbol{\sigma}\, dV, \quad \boldsymbol{D} = \frac{1}{|\Omega|}\int_\Omega \boldsymbol{d}\,\mathrm{d}V \tag{11}$$

where $|\Omega|$ is the cell volume. In the case of uniform natural boundary conditions, another upscaling bridge between both microscopic ($\boldsymbol{\sigma}$) and macroscopic ($\boldsymbol{\Sigma}$) stress fields can be established [46, 47]:

$$\boldsymbol{\sigma n} = \boldsymbol{\Sigma n} \text{ on } \partial\Omega \tag{12}$$

where $\boldsymbol{n}$ is the outward unit normal vector at a given point on the boundary $\partial\Omega$. Reasoning on the problem presented in Fig. 1, supposing that a uniform radial stress Σ_r is imposed on the outer boundary ($r = b$) and a stress-free void surface ($r = a$), relation (12) implies that:

$$\sigma_r(r = b) = \Sigma_r \quad \text{and} \quad \sigma_r(r = a) = 0 \tag{13}$$

where σ_r is the microscopic radial stress.

The set of kinematically admissible velocity fields $\boldsymbol{v}$ is given by:

$$\mathcal{K}_a = \{\boldsymbol{v} \text{ s.t. } \boldsymbol{v}(\boldsymbol{x}) = \boldsymbol{D}\boldsymbol{x} \text{ on } \partial\Omega\} \tag{14}$$

where $\boldsymbol{x}$ is the position vector. The set of statically admissible stress fields is defined as:

$$\mathcal{S}_a = \{\boldsymbol{\sigma} \text{ s.t. } \text{div}\boldsymbol{\sigma} = \boldsymbol{0} \text{ in } \Omega,\ \boldsymbol{\sigma}\boldsymbol{n} = \boldsymbol{0} \text{ on } \partial\omega,\ \boldsymbol{\sigma} = \boldsymbol{0} \text{ in } \omega\} \tag{15}$$

where $\boldsymbol{n}$ is the unit outward normal vector.

It has been shown that the variational homogenization is equivalent to solve the following minimization problem under the constraint $\phi(\boldsymbol{\sigma}) = 0$ [4, 47]:

$$\underset{\boldsymbol{\sigma}\in\mathcal{S}_y}{min}(-\boldsymbol{\Sigma} : \boldsymbol{D}) \tag{16}$$

where

$$\mathcal{S}_y = \{\boldsymbol{\sigma} \in \mathcal{S}_a \text{ s.t. } \phi(\boldsymbol{\sigma}) \leq 0 \text{ a.e. in } \Omega_m\} \tag{17}$$

defines the admissible stress space. However, as it has been discussed by Cheng et al. [8] and Shen et al. [37, 43], due to the difficult in satisfying the constraint $\phi(\boldsymbol{\sigma}) = 0$ at every point in the matrix material domain Ω_m, this condition is enforced only in the average sense. Therefore, using a Lagrange multiplier $\dot{\Lambda} \geq 0$ (homogeneous in Ω_m), the constrained minimization is replaced by an equivalent saddle-point problem given in terms of the Lagrangian functional $\mathcal{L}(\boldsymbol{\sigma}, \dot{\Lambda}) = \frac{\dot{\Lambda}}{|\Omega|}\int_{\Omega_m}\phi(\boldsymbol{\sigma})dV - \boldsymbol{\Sigma} : \boldsymbol{D}$:

$$\underset{\dot{\Lambda}\geq 0}{max}\,\underset{\boldsymbol{\sigma}\in\mathcal{S}_a}{min}\left(\mathcal{L}(\boldsymbol{\sigma}, \dot{\Lambda}) = \frac{\dot{\Lambda}}{|\Omega|}\int_{\Omega_m}\phi(\boldsymbol{\sigma})dV - \boldsymbol{\Sigma} : \boldsymbol{D}\right) \tag{18}$$

where the macroscopic strength criterion reads:

$$\Phi(\boldsymbol{\Sigma}) = \frac{1}{|\Omega|}\int_{\Omega_m}\phi(\boldsymbol{\sigma}(\boldsymbol{\Sigma}))dV = 0 \tag{19}$$

Thereby, the saddle-point problem becomes [8]:

$$\underset{\dot{\Lambda}\geq 0}{max}\,\underset{\boldsymbol{\Sigma}}{min}\left(\mathcal{L}(\boldsymbol{\Sigma}, \dot{\Lambda}) = \dot{\Lambda}\Phi(\boldsymbol{\Sigma}) - \boldsymbol{\Sigma} : \boldsymbol{D}\right) \tag{20}$$

Accordingly, the solution of the previous problem results in an associative macroscopic plastic flow rule $\boldsymbol{D} = \dot{\Lambda}\frac{\partial\Phi}{\partial\boldsymbol{\Sigma}}$ and the macroscopic Kuhn-Tucker loading-unloading conditions, $\dot{\Lambda} \geq 0$, $\Phi(\boldsymbol{\Sigma}) \leq 0$, and $\dot{\Lambda}\Phi(\boldsymbol{\Sigma}) = 0$. To be highlighted that the problem stated in (20) resembles to the maximum dissipation principle at the macroscopic scale, also resulting in the *convexity* of the macroscopic yield function [4, 13, 18, 31].

3.1 Microscopic and macroscopic trial stress fields

In order to obtain the macroscopic strength criterion, the next key step is to build-up an admissible microscopic trial stress field $\boldsymbol{\sigma}$ [8, 37, 43]. Thereby, the macroscopic stress tensor $\boldsymbol{\Sigma}$ can be obtained using the average relation stated in Eq. $(11)_1$ and/or the uniform traction condition given in Eq. (12), which was particularized in Eq. (13) considering the axisymmetric cylindrical problem given in Fig. 1.

Following the rationale of Cheng et al. [8] and Shen et al. [37], the trial stress field $\boldsymbol{\sigma}$ is assumed to be given by the sum of two stress tensor fields:

$$\boldsymbol{\sigma} = \boldsymbol{\sigma}_1 + \boldsymbol{\sigma}_2 \tag{21}$$

The first one is obtained based on the analytical solution developed by Monchiet and Kondo [30] to a plastic hollow sphere with a Mises–Schleicher matrix material. The development of Monchiet and Kondo [30] is extended to the case of a hollow cylinder, thus resulting in the following stress solution (see Eqs. (A.12)–(A.14) in Appendix A for more details):

$$\sigma_{1r} = \frac{A_1}{3\alpha}\left[1 - \frac{3\alpha^2}{4}W^2\left(p\frac{a^2}{r^2}\right) - \frac{3\alpha^2}{2}W\left(p\frac{a^2}{r^2}\right)\right] \tag{22}$$

$$\sigma_{1\theta} = \frac{A_1}{3\alpha}\left[1 - \frac{3\alpha^2}{4}W^2\left(p\frac{a^2}{r^2}\right) + \frac{3\alpha^2}{2}W\left(p\frac{a^2}{r^2}\right)\right] \tag{23}$$

$$\sigma_{1z} = \frac{A_1}{3\alpha}\left[1 - \frac{3\alpha^2}{4}W^2\left(p\frac{a^2}{r^2}\right)\right] \tag{24}$$

where $A_1 > 0$ is a constant, which satisfies $A_1 = \sigma_0$ for a purely hydrostatic loading. Therefore, considering the trial radial stress given in Eq. (22) into Eq. $(13)_1$, the first macroscopic radial stress reads:

$$\Sigma_{1r} = \frac{A_1}{3\alpha}\left[1 - \frac{3\alpha^2}{4}W^2(pf) - \frac{3\alpha^2}{2}W(pf)\right] \tag{25}$$

where relation $f = \frac{a^2}{b^2}$ has been used and parameter p is given in Eq. (A.16).

Furthermore, the macroscopic longitudinal stress can be calculated using the average relation $(11)_1$ considering the trial stress given in Eq. (24):

$$\Sigma_{1z} = \frac{1}{|\Omega|}\frac{A_1}{3\alpha}\int_{-\frac{H}{2}}^{\frac{H}{2}}\int_0^{2\pi}\int_a^b r\left[1 - \frac{3\alpha^2}{4}W^2\left(p\frac{a^2}{r^2}\right)\right]dr d\theta \mathrm{d}z \tag{26}$$

where $\mathrm{d}v = r\mathrm{d}r\mathrm{d}\theta\mathrm{d}z$ denotes an infinitesimal volume element in cylindrical coordinates. Previous integral results in:

$$\Sigma_{1z} = \frac{A_1}{3\alpha}\left[1 - \frac{3\alpha^2}{4}W^2(pf) - \frac{3\alpha^2}{2}W(pf)\right] \tag{27}$$

where relations $|\Omega| = H\pi b^2$, $f = \frac{a^2}{b^2}$ and condition (A.15) have been employed. Comparing Eqs. (25) and (27), it is easily noticed that $\Sigma_{1z} = \Sigma_{1r}$.

Due to axisymmetry of the problem considered here (see Fig. 1), the first macroscopic stress tensor $\boldsymbol{\Sigma}_1$ can be written in Cartesian coordinates based on the following relations: $\Sigma_r = \Sigma_1 = \Sigma_2$ and $\Sigma_z = \Sigma_3$. Therefore, using Eqs. (25) and (27), the first macroscopic stress tensor is obtained:

$$\boldsymbol{\Sigma}_1 = \frac{A_1}{3\alpha}\left(1 + \frac{3\alpha^2}{4}\Upsilon\right)(\boldsymbol{e}_1 \otimes \boldsymbol{e}_1 + \boldsymbol{e}_2 \otimes \boldsymbol{e}_2 + \boldsymbol{e}_3 \otimes \boldsymbol{e}_3) \tag{28}$$

where the following parameter was defined:

$$\Upsilon = -W^2(pf) - 2W(pf) \tag{29}$$

As it can be readily seen in Eq. (28), the first microscopic trial stress field adopted in Eqs. (22)–(24) results in a purely hydrostatic macroscopic stress tensor.

The second microscopic trial stress field $\boldsymbol{\sigma}_2$ results from the solution derived in Appendix B, where a purely uniform longitudinal loading is considered. Therefore, based on Eqs. (B.1) and (B.4), $\boldsymbol{\sigma}_2$ is given by:

$$\boldsymbol{\sigma}_2 = A_2 \boldsymbol{e}_z \otimes \boldsymbol{e}_z \tag{30}$$

where A_2 is a constant. For a pure longitudinal loading, $A_2 = \frac{1}{2}\left(-\alpha \pm \sqrt{\alpha^2 + 4}\right)\sigma_0$, see Eq. (B.4). That is, constant A_2 depends on whether a tensile or a compressive load is imposed. It is worth emphasizing that both stress fields, $\boldsymbol{\sigma}_1$ and $\boldsymbol{\sigma}_2$, satisfy the stress-free condition $\boldsymbol{\sigma n} = \boldsymbol{0}$ at the cavity wall (see Eq. $(13)_2$). Therefore, the microscopic trial stress field adopted in this work complies with all the conditions related to the statically admissible stress set defined in Eq. (15).

Inserting Eq. (30) into Eq. $(11)_1$, and using relations $|\Omega| = H\pi b^2$ and $f = \frac{a^2}{b^2}$, the second macroscopic stress field is obtained:

$$\boldsymbol{\Sigma}_2 = \frac{A_2}{|\Omega|} \int_{-\frac{H}{2}}^{\frac{H}{2}} \int_0^{2\pi} \int_a^b r \mathrm{d}r \mathrm{d}\theta \mathrm{d}z \boldsymbol{e}_z \otimes \boldsymbol{e}_z$$

providing

$$\boldsymbol{\Sigma}_2 = (1-f) A_2 \boldsymbol{e}_3 \otimes \boldsymbol{e}_3 \tag{31}$$

which was given in Cartesian coordinates for future convenience, remembering that X_3 is parallel to z (see Fig. 1).

3.2 Macroscopic yield criterion

Considering the macroscopic stress tensors given in Eqs. (28) and (31), the total macroscopic stress tensor is then obtained according to the following superposition: $\boldsymbol{\Sigma} = \boldsymbol{\Sigma}_1 + \boldsymbol{\Sigma}_2$. Based on the macroscopic stress tensor, we calculate an *equivalent shear stress* (Σ_{sh}) and the *mean lateral stress* (Σ_m), respectively by:

$$\Sigma_{sh} = \Sigma_3 - \Sigma_1 = (1-f) A_2 \tag{32}$$

and

$$\Sigma_m = \frac{1}{2}(\Sigma_1 + \Sigma_2) = \frac{A_1}{3\alpha}\left(1 + \frac{3\alpha^2}{4}\Upsilon\right) \tag{33}$$

Notice that, the equivalent shear stress Σ_{sh} relates to the equivalent von Mises stress Σ_e according to: $\Sigma_e = |\Sigma_{sh}|$ or $\Sigma_{sh} = \Sigma_e \mathrm{sign}(\sigma_3 - \sigma_1)$. In addition, for the axisymmetric loading considered in this work (see Fig. 1), the mean lateral stress Σ_m, which is responsible for the cylindrical void growth [2, 17], is equal to the radial stress Σ_r given in Eq. (25), therefore: $\Sigma_m = \Sigma_1$, since $\Sigma_r = \Sigma_1 = \Sigma_2$ in this case.

From Eqs. (3) and (19), the macroscopic yield function can be obtained considering the superposition (21), and the microscopic trial stress fields given in Eqs. (22)–(24) and (30), leading to (for more details, we refer to Appendix C):

$$\Phi(\boldsymbol{\Sigma}) = -\left(f + \frac{3\alpha^2}{4}\Upsilon\right) A_1^2 + A_2^2(1-f) + \sigma_0\left(1 + \frac{3}{4}\alpha^2\Upsilon\right) A_1 + (1-f)\alpha\sigma_0 A_2 - (1-f)\sigma_0^2 = 0 \tag{34}$$

Thus, using Eqs. (32) and (33), the macroscopic yield function is obtained:

$$\Phi(\boldsymbol{\Sigma}) = \frac{\Sigma_{sh}^2}{\sigma_0^2} - \Theta\frac{\Sigma_m^2}{\sigma_0^2} + \alpha(1-f)\frac{(3\Sigma_m + \Sigma_{sh})}{\sigma_0} - (1-f)^2 = 0 \tag{35}$$

being

$$\Theta = \frac{9\alpha^2(1-f)\left(f + \frac{3\alpha^2}{4}\Upsilon\right)}{\left(1 + \frac{3\alpha^2}{4}\Upsilon\right)^2} \tag{36}$$

where parameters α, σ_0 and Υ are given in Eqs. (2) and (29), respectively. Notice that parameter p in Eq. (29) is calculated using Eq. (A.16) and it has two branches: p_+ for positive values of Σ_m and p_- for negative values of Σ_m. Furthermore, it is noticed in Eq. (35) that the sign of both Σ_m and Σ_{sh} play important roles in this macroscopic yield criterion, leading to an asymmetric yield locus in the Σ_{sh}-Σ_m stress space (see for instance Figs. 4 and 5). It is observed that the tension–compression asymmetry of the matrix is the main source of this behavior. That is, unless the special condition leading to a von Mises matrix ($\alpha = 0$ or $k = 1$) is considered, the yield locus is not symmetric with respect to the Σ_m-axis or Σ_{sh}-axis.

Overall, Eq. (35) provides an approximate yield surface depending on the current material porosity f, the tension–compression material asymmetry α, the macroscopic mean lateral stress Σ_m (Eq. (33)), and an equivalent shear stress Σ_{sh} (Eq. (32)). Moreover, using the fact that $W(0) = 0$ in Eqs. (29) and (36), knowing that $3\Sigma_h = 2\Sigma_1 + \Sigma_3$, Σ_h being the macroscopic hydrostatic stress, Eq. (35) recovers the yield criterion of the matrix material given in Eq. (3) when $f = 0$.

3.2.1 Particular case of a von Mises matrix material

For the particular case of a von Mises matrix material, parameter α in Eq. (3) has to be set equal to zero. Thus, in order to obtain the particular forms of Eq. (35) to the case of a von Mises matrix, Taylor expansions of the Lambert function, $W(fp_+)$ and $W(fp_-)$, at $\alpha \to 0$ ($k \to 1$) are used (see also Monchiet and Kondo [30]):

$$W(fp_+) = \sqrt{\frac{4}{3}\frac{1}{\alpha}} + \ln(f) - 1 + o(\alpha) \tag{37}$$

$$W(fp_-) = -\sqrt{\frac{4}{3}\frac{1}{\alpha}} + \ln(f) - 1 + o(\alpha) \tag{38}$$

Therefore, using Eq. (37), for $\Sigma_m \geq 0$ (or Eq. (38), for $\Sigma_m \leq 0$), in Eqs. (29) and (36), the yield criterion of Eq. (35) becomes:

$$\Phi(\boldsymbol{\Sigma}) = \frac{\Sigma_{sh}^2}{\sigma_0^2} + \frac{3(1-f)^2}{\ln^2(f)}\frac{\Sigma_m^2}{\sigma_0^2} - (1-f)^2 = 0 \text{ for } \alpha \to 0 \tag{39}$$

It is important to mention that when $\alpha \to 0$, the yield criterion does not depend either on the sing of Σ_{sh} nor the sign of Σ_m. That is, the yield surface is symmetric with respect to both the Σ_{sh} and Σ_m axes. However, in an overall sense, Eq. (35) does not recover Gurson's model when $\alpha \to 0$.

For a particular case in which $\Sigma_{sh} = 0$ and $\Sigma_m > 0$ (hydrostatic stress state with void expansion), Eq. (39) provides:

$$\Sigma_m = -\frac{\ln(f)}{\sqrt{3}}\sigma_0 \text{ for } \alpha \to 0 \tag{40}$$

Similarly, for $\Sigma_{sh} = 0$ and $\Sigma_m < 0$ (hydrostatic stress state with void reduction), Eq. (39) yields:

$$\Sigma_m = \frac{\ln(f)}{\sqrt{3}}\sigma_0 \text{ for } \alpha \to 0 \tag{41}$$

It is clearly seen that the developed model (Eq. (35)) recovers the exact Gurson's solution (Eq. (C.2)) when a purely hydrostatic loading is employed and parameter $\alpha \to 0$ is set.

4 Finite element model

The theoretical model developed in this work is verified against Finite Element (FE) calculations. Numerical simulations consist of cell analysis that are performed in the commercial software [1]. The numerical model used in this work is an axisymmetric bidimensional voided cell with initial hight H_0, inner and outer radius a_0 and b_0, respectively. The initial ratio between H_0 and b_0 is chosen to be $H_0/b_0 = 4$. Symmetry about X_1-axis is imposed so that only half of the cell is considered in the numerical analysis. Finite element discretization is performed using 40 CAX8R elements. Both boundary conditions and finite element discretization are shown in Fig. 2. The boundary conditions applied along the outer faces of the cell are:

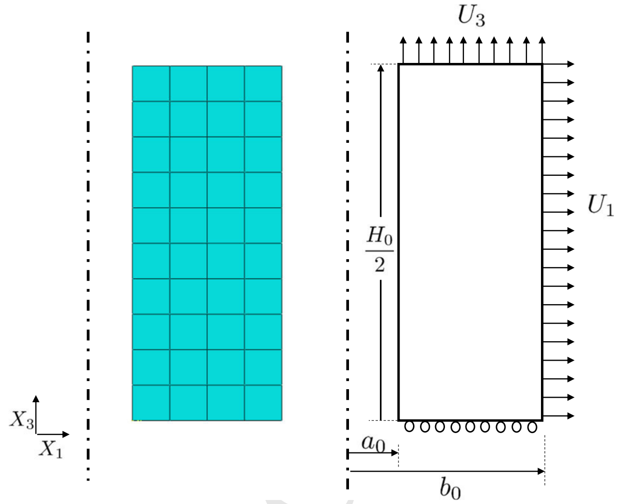

Fig. 2 Finite element discretization and boundary conditions applied to the axisymmetric cylindrical cell

$$\begin{aligned} u_1 &= U_1, \quad \text{for} \quad X_1 = b; \qquad & u_1 &= 0, \quad \text{for} \quad X_1 = 0 \\ u_3 &= U_3, \quad \text{for} \quad X_3 = H/2; \qquad & u_3 &= 0, \quad \text{for} \quad X_3 = 0 \end{aligned}$$

where U_1 and U_3 are prescribed displacements in radial and longitudinal directions, respectively. The displacements, U_1 and U_3, are imposed such that the corresponding average macroscopic stresses (see also Eqs. (11)$_1$ and (12)),

$$\Sigma_1 = \frac{2}{H} \int_0^{H/2} [\sigma_1]_{X_1=b} \, dX_3; \quad \Sigma_3 = \frac{2}{b^2} \int_0^{b} [\sigma_3]_{X_3=H/2} \, X_1 \mathrm{d}X_1 \tag{42}$$

have proportional values during the whole loading history. In Eq. (42), σ_1 and σ_3 are the Cauchy stress components, $b = b_0 + U_1$ and $H/2 = H_0/2 + U_3$ are the current outer radius and length of the cylinder, respectively. Simulations are carried out employing a MPC (Multi-Point Constraints) user subroutine, in which displacement boundary conditions are imposed, while constant macroscopic stress triaxialities ($T = \Sigma_h/|\Sigma_{sh}|$) are ensured during deformation. On the one hand, since continuous displacement and velocity fields are developed, Pastor et al. [32] emphasized that standard FE approach cannot be qualified in terms of bounds, except for very special homogeneous problems. On the other hand, Cheng et al. [8] reported results showing that MPC-based cell analysis, using standard FE simulations, provides results between upper and lower numerical bounds (see for instance numerical limit analysis developed by Trillat and Pastor [48] and Pastor et al. [34]). In this sense, MPC-based numerical simulations are expected to provide suitable reference solutions to compare the stress-based theoretical model with, as it has been done in Cheng et al. [8]. For further details on the MPC-based strategy used to prescribe boundary conditions, we refer to Cheng and Guo [7] and Vadillo and Fernández–Sáez [51].

In the FE model, the matrix material is described according to the constitutive model provided in Sect. 2. The set of non-linear constitutive equations is solved implicitly within the finite element framework at the material level. The algorithm is implemented in ABAQUS/Standard [1] via a UMAT user subroutine. More details on the numerical formulation and its implementation can be found in Vadillo et al. [52]. While a hypo-elastic finite strain framework has been adopted, in the numerical simulations performed in this work, both initial and final void volume fraction were practically the same. This is due to the fact that the maximum displacement imposed on the external faces, in order to yield the whole cell, was less than $10^{-5} H_0$. Therefore, a small strain framework could have been used in the numerical cell analysis.

5 Results

In this section, the predictions of the constitutive model presented in Eq. (35) are compared with the results given by numerical simulations. The numerical simulations are carried out for a Mises–Schleicher–Burzyński

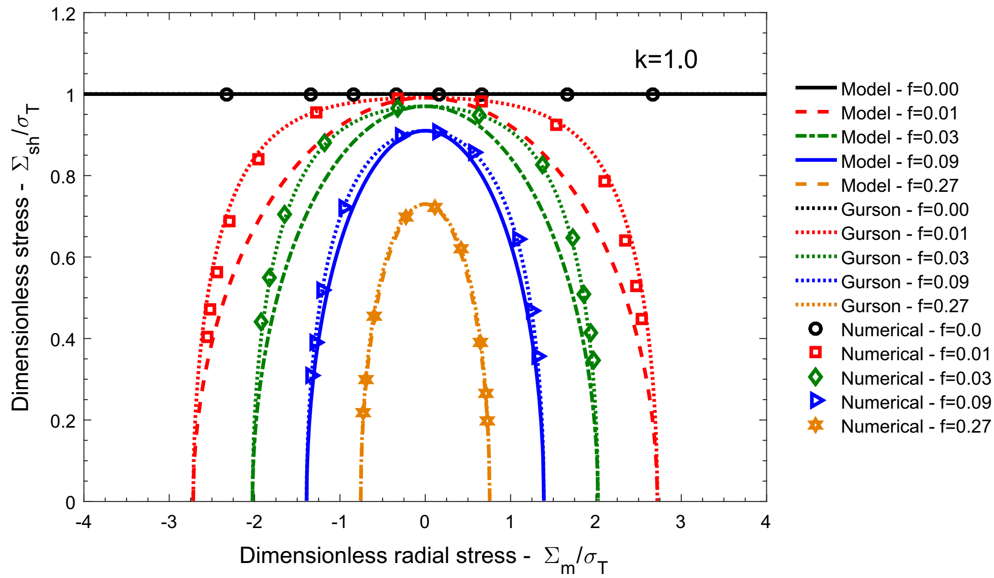

Fig. 3 Comparison between the developed model (Eq. (39)), criterion of Gurson [17] (Eq. (C.1)) and finite element results for $k = 1.0$ and different material porosities $f = (0.00,\ 0.01,\ 0.03,\ 0.09,\ 0.27)$: yield surfaces plotted in the plane of the dimensionless equivalent shear stress Σ_{sh}/σ_T *versus* the dimensionless mean lateral stress Σ_m/σ_T. Notice that, for the axisymmetric cylindrical case shown in Fig. 1c, we have $\Sigma_{sh} = \Sigma_3 - \Sigma_1$ and $\Sigma_m = \Sigma_1 = \Sigma_2$

material with $E = 7170.8$ GPa, $\sigma_T = 384.05$ MPa, $\nu = 0.33$ and $k = 1.0,\ 1.2,\ 1.5$. In the numerical hollow cylinder, the ratios of a_0 and b_0 are chosen in such a way that $f_0 = a_0^2/b_0^2 = 0.01,\ 0.03,\ 0.09,\ 0.27$. The range of macroscopic triaxiality values ($T = \Sigma_h/|\Sigma_{sh}|$) analysed varies from $T = -50$ up to $T = 6$ for $\Sigma_{sh} < 0$ ($\Sigma_1 > \Sigma_3$) and $\Sigma_{sh} > 0$ ($\Sigma_1 < \Sigma_3$). The yield functions will be presented in the Σ_{sh}/σ_T-Σ_m/σ_T dimensionless stress space. It is worth mentioning that, for all values of f and k considered in the analyses, *convex* yield functions have been obtained from Eq. (35). To be emphasized that, while a wide range of the void volume fraction has been considered in this parametric study, phenomena such as internal necking and void coalescence are not taken into account in our development. However, we are aware that such failure mechanisms are expected to play important roles in the failure of porous materials (see for instance the review paper of Benzerga and Leblond [2]).

Figure 3 shows the yield surfaces predicted by the developed criterion (Eq. (39)) for $k = 1.0$, ($\sigma_C = \sigma_T = \sigma_0$), in comparison with the results given by the finite element simulations (symbols). The yield surfaces for $k = 1.0$ exhibits symmetry with respect to both the Σ_m and Σ_{sh} axes, thus only positive values of $\Sigma_{sh} = (\Sigma_3 - \Sigma_1)$ are presented in the figure. For $k = 1.0$, the Mises–Schleicher–Burzynski model reduces to the von Mises yield function. As it is well known, for a voided cylindrical cell with a perfectly plastic von Mises matrix material, the analytical expression of the yield criterion has the solution given by Gurson [17] (see Eq. (C.1)). For $f = 0$ (no void in the cell) all 3 criteria are coincident. For $f = 0.01$ and $f = 0.03$, there are some differences between the proposed model, the numerical results given by the simulations and the analytical solution given by Gurson's model (dotted lines). These differences are higher for $f = 0.01$ than for $f = 0.03$ and vanish when $\Sigma_{sh} = 0$ ($T = \pm\infty$) and $\Sigma_m = 0$ ($T = \pm 1/3$). The highest difference between Σ_{sh} obtained numerically and analytically, for a fixed value of Σ_m, is $\sim 14\,\%$ for $\Sigma_m/\sigma_T = -1.96$ ($T \approx -2$) when $f = 0.01$. However, it is observed that, for higher porosity values ($f = 0.09$, $f = 0.27$) and all the stress states considered, there is an excellent agreement between the proposed yield function, Gurson's criterion and numerical results.

It is noticed in Fig. 3 that the proposed model always provide yield surfaces that are below those obtained from Gurson's model. This behavior should be expected since Gurson's model consists of a kinematic limit analysis, which is known to provide upper bounds [23]. In contrast, the stress-based approach of Cheng et al. [8] is reported to provide quasi-lower bounds. Nevertheless, the proposed model is expected to provide exact solutions for either a purely hydrostatic loading, $T = \pm\infty$, (see Appendix A) or a homogeneous longitudinal stress field, $T = \pm 1/3$ (see Appendix B). Similar trends have also been reported in Cheng et al. [8], in the sense that Gurson's yield curves were slightly above MPC-based finite element simulations and their stress-based

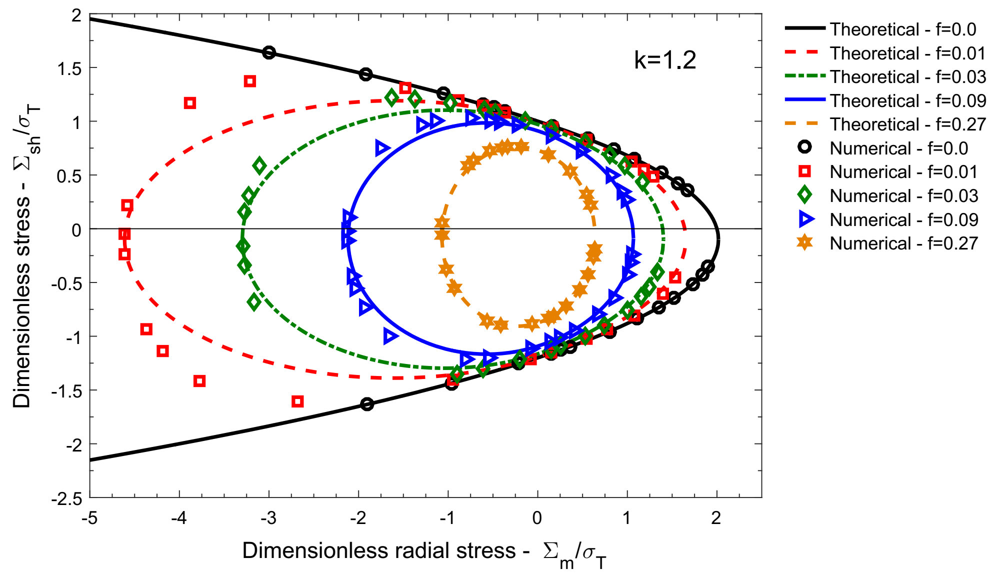

Fig. 4 Comparison between the developed model (Eq. (35)) and finite element results for $k = 1.2$ and different material porosities $f = (0.00, 0.01, 0.03, 0.09, 0.27)$: yield surfaces plotted in the plane of the dimensionless equivalent shear stress Σ_{sh}/σ_T *versus* the dimensionless mean lateral stress Σ_m/σ_T. Notice that, for the axisymmetric cylindrical case shown in Fig. 1c, we have $\Sigma_{sh} = \Sigma_3 - \Sigma_1$ and $\Sigma_m = \Sigma_1 = \Sigma_2$

model has always provided curves below the numerical results. However, the three approaches coincided for both purely hydrostatic and pure shear loading.

A comparison of the analytical solution according to Eq. (35) and the finite element results for $k = 1.2$ is shown in Fig. 4. Although the yield surface for the dense material ($f = 0.0$) is open when Σ_m is negative, the yield surfaces for $f > 0$ are closed. As expected, the porous yield stress becomes smaller as the porosity f increases and always falls within the envelope of the yield surface for $f = 0.0$. As it can be seen in Fig. 4, in contrast to the case with $k = 1.0$ (Fig. 3), the yield surface is asymmetric with respect to both the Σ_m and Σ_{sh} axes. Taking the numerical results as reference, the lower bound nature of the proposed yield surface is clearly observed from the figure, being the analytical solution from Eq. (35) slightly lower than numerical results and overlapping both (numerical and analytical) results for purely hydrostatic loading and for $\Sigma_m = 0$. The largest differences between both theoretical and numerical results are observed for $f = 0.01$ and negative values of Σ_m. The maximum difference is found to be in the order of 28 % for $\Sigma_m/\sigma_T = -3.2$ ($T \approx -2$) when $f = 0.01$.

Figure 5 compares the predicted yield locus with numerical data for $k = 1.5$. The analytical yield functions capture the numerical set quite well. As in the case with $k = 1.2$, for $k = 1.5$, the analytical results are in better agreement with numerical values for $f = 0.0$ and for the highest values of f analysed. For $f = 0.01$, 0.03 and $\Sigma_m < 0$, the numerical results are not perfectly met. For all porosities, both theoretical and numerical solutions overlap each other when either $\Sigma_{sh} = 0$ or $\Sigma_m = 0$. It was found that the maximum difference is 31 % for $\Sigma_m/\sigma_T = -5.38$ ($T \approx -2$) when $f = 0.01$.

Overall, for all values of k considered in this study, the highest differences between the theoretical and numerical results have been observed for $f = 0.01$ with stress triaxiliaties close to -2. In the present approach, the microscopic stress fields resulting in either a purely hydrostatic macroscopic stress state ($T = \pm\infty$) or a longitudinal loading ($T = \pm 1/3$) have been considered. Therefore, the trial stress field has been obtained from the superposition of both of them (Eq. (21)). However, if another stress solution, for an intermediate value of T, can be obtained, the theoretical model could be enriched and thus provide predictions closer to the reference results.

Aiming at evidencing the influence of the matrix asymmetry parameter k on the predicted yield surface, Figs. 6, 7, 8, 9 and 10 also compare the proposed model (Eq. (35)) with finite element simulations. However, now comparisons are performed keeping the material porosity f constant and varying the value of k. In addition, in order to check the predictive capability of the proposed criterion when compared to other approaches, yield surfaces obtained using the model of Lee and Oung [24] for cylindrical voids (see Eq. (C.7)) are also shown in those figures.

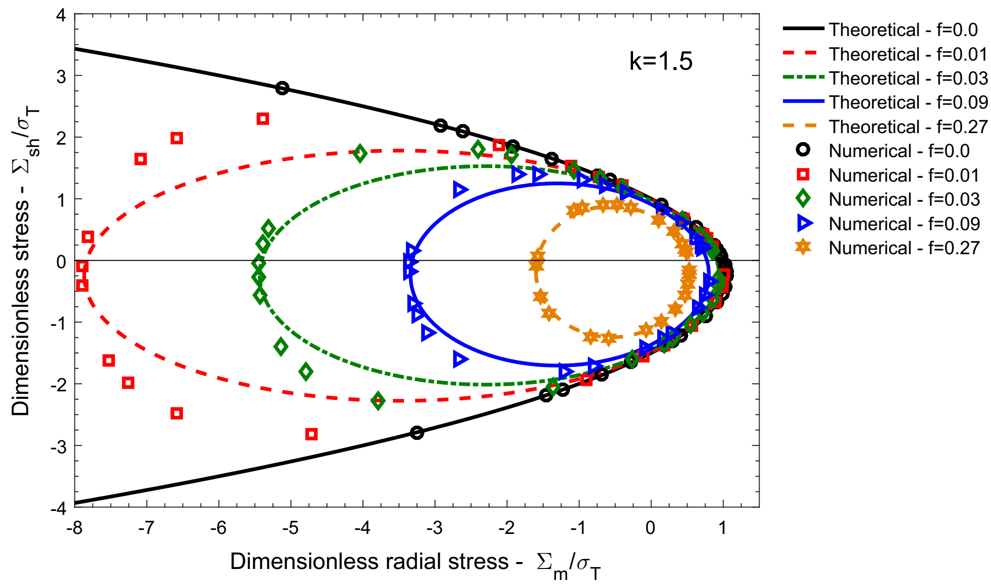

Fig. 5 Comparison between the developed model (Eq. (35)) and finite element results for $k = 1.5$, and different material porosities $f = (0.00,\ 0.01,\ 0.03,\ 0.09,\ 0.27)$: yield surfaces plotted in the plane of the dimensionless equivalent shear stress Σ_{sh}/σ_T *versus* the dimensionless mean lateral stress Σ_m/σ_T. Notice that, for the axisymmetric cylindrical case shown in Fig. 1c, we have $\Sigma_{sh} = \Sigma_3 - \Sigma_1$ and $\Sigma_m = \Sigma_1 = \Sigma_2$

Figure 6 compares the theoretical predictions, using Eq. (3) (dense material), with finite element simulations considering a material porosity $f = 0.0$ and different values of the asymmetry parameter: $k = 1.0,\ 1.2,\ 1.5$. It is readily seen that the pressure sensitivity of the material increases as k does. On the one hand, for $\Sigma_m > 0$, higher values of k lead to smaller yield domains. On the other hand, when $\Sigma_m < 0$, the opposite behavior is evidenced (asymmetry with respect to the Σ_{sh}-axis). Furthermore, the asymmetry of the yield locus with respect to the Σ_m-axis also increases with k, such that the elastic domain is translated downward. It is observed in Fig. 6 that, for $k > 0$, the yield locus is asymmetric with respect to both the Σ_m and Σ_{sh} axes for dense materials. This behavior is observed because Eq. (35) depends on the sign of Σ_{sh} and Σ_m even when $f = 0$. Notice that the matrix yield criterion (Eq. (3)) is symmetric with respect to the hydrostatic stress (Σ_h) axis and not to the lateral mean stress (Σ_m).

Figure 7 shows the yield functions for $f = 0.01$ and distinct values of parameter k. As it would be expected, the results also show that the asymmetry of the curves is more pronounced for higher values of k. For $k = 1.0$ (von Mises matrix), Lee and Oung's model (that recovers Gurson's model when $k = 1.0$) provides a better agreement with numerical results when compared with the present approach (see also discussion on Fig. 3). However, as k increases (for $k = 1.2$ and $k = 1.5$), both theoretical approaches (Eqs. (35) and (C.6)) provide adequate results for positive values of Σ_m. In contrast, both theoretical models underestimate the numerical yield function when $\Sigma_m < 0$. However, for purely (negative) hydrostatic stress state, the proposed model (Eq. (35)) is in excellent agreement with the numerical counterpart. Both the finite element results and the yield criterion proposed here cross the negative branch of the Σ_m-axis at the points $(-2.64,\ 0)$ for $k = 1.0$, $(-4.60,\ 0)$ for $k = 1.2$ and $(-7.80,\ 0)$ for $k = 1.5$. Furthermore, it is readily seen in Fig. 7 that the yield curves obtained using Lee and Oung's model (Eq. (C.6)) strongly underestimate the reference results. The intersections with the negative branch of the Σ_m-axis are at: $(-2.64,\ 0)$ for $k = 1.0$, $(-3.53,\ 0)$ for $k = 1.2$ and $(-4.42,\ 0)$ for $k = 1.5$. Except for the case with $k = 1.0$, the analytical model developed in this work provides better predictions when compared with Lee and Oung's proposal.

As it is shown in Fig. 8, the same behavior observed for $f = 0.01$ (Fig. 7) is exhibited when $f = 0.03$. Results demonstrate that the proposed model provides good approximations when positive values of Σ_m are considered. However, it underestimates the effective response of the material for negative values of Σ_m. The discrepancies decrease gradually as purely hydrostatic stress states are approached ($\Sigma_{sh} = 0$). Slightly higher differences are found when higher values of k are set. In addition, similarly to case with $f = 0.01$, if the whole stress range is considered, the analytical model proposed here gives better predictions when compared with Lee and Oung's model.

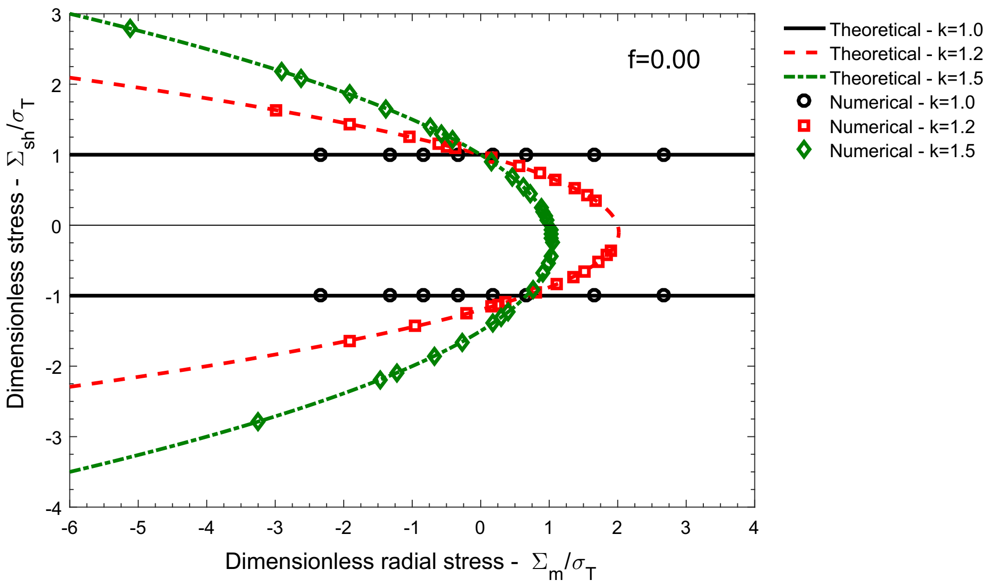

Fig. 6 Comparison between the developed model (Eq. (35)), the approximate criterion of Lee and Oung [24] (Eq. C.6) and finite element results for $f = 0.00$ and different values of parameter $k = (1.0, 1.2, 1.5)$: yield surfaces plotted in the plane of the dimensionless equivalent shear stress Σ_{sh}/σ_T *versus* the dimensionless mean lateral stress Σ_m/σ_T. Notice that, for the axisymmetric cylindrical case shown in Fig. 1c, we have $\Sigma_{sh} = \Sigma_3 - \Sigma_1$ and $\Sigma_m = \Sigma_1 = \Sigma_2$

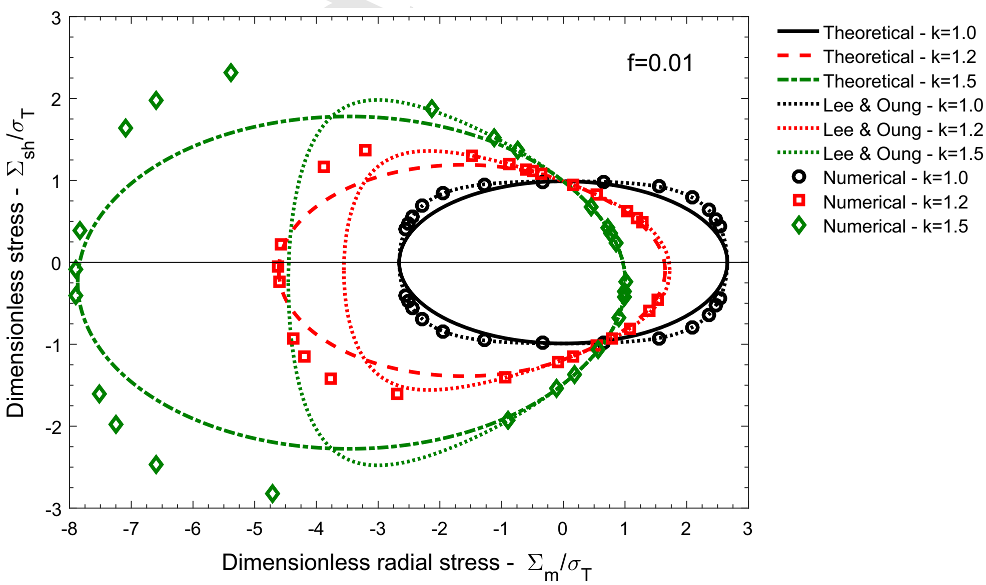

Fig. 7 Comparison between theoretical (Eq. (35)), the approximate criterion of Lee and Oung [24] (Eq. C.6) and finite element results for $f = 0.01$ and different values of parameter $k = (1.0, 1.2, 1.5)$: yield surfaces plotted in the plane of the dimensionless equivalent shear stress Σ_{sh}/σ_T *versus* the dimensionless mean lateral stress Σ_m/σ_T. Notice that, for the axisymmetric cylindrical case shown in Fig. 1c, we have $\Sigma_{sh} = \Sigma_3 - \Sigma_1$ and $\Sigma_m = \Sigma_1 = \Sigma_2$

Similar trends are observed for $f = 0.09$ and $f = 0.27$ (see Figs. 9 and 10). It is also noticed that if the porosity value is higher, the predicted material response is closer to the reference data. Particularly, as it can be seen in Fig. 10, the present analytical approach and the numerical solutions are closely overlapping for $f = 0.27$ for all values of k considered here.

Overall, analysis of Figs. 7, 8, 9 and 10 shows that the asymmetry with respect to both the Σ_m and Σ_{sh} axes increases with k. In addition, the proposed model provides lower estimative for the yield surface when compared to the finite element results. However, while the differences increase with k, the discrepancies decrease as the

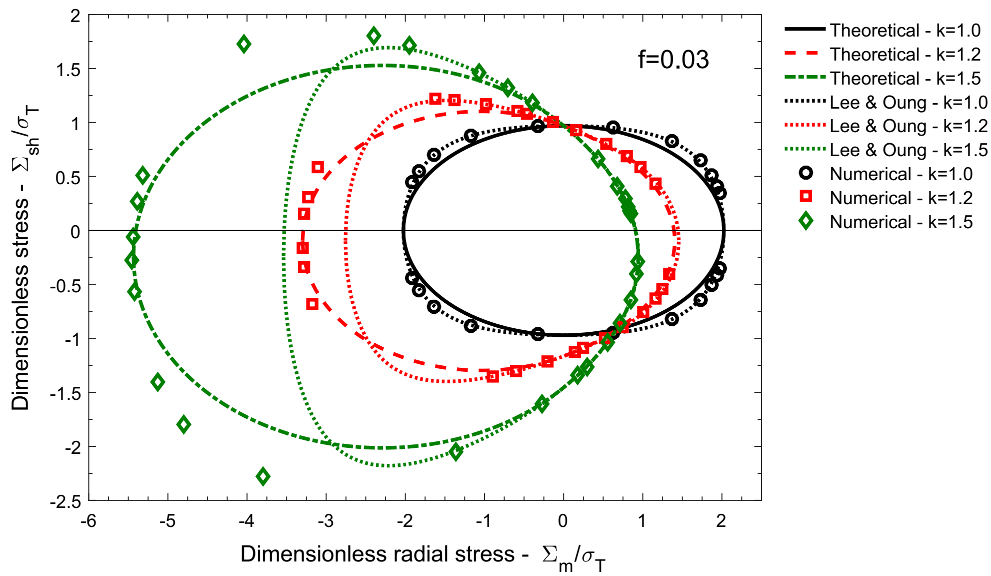

Fig. 8 Comparison between theoretical (Eq. (35)), the approximate criterion of Lee and Oung [24] (Eq. C.6) and finite element results for $f = 0.03$ and different values of parameter $k = (1.0,\ 1.2,\ 1.5)$: yield surfaces plotted in the plane of the dimensionless equivalent shear stress Σ_{sh}/σ_T *versus* the dimensionless mean lateral stress Σ_m/σ_T. Notice that, for the axisymmetric cylindrical case shown in Fig. 1c, we have $\Sigma_{sh} = \Sigma_3 - \Sigma_1$ and $\Sigma_m = \Sigma_1 = \Sigma_2$

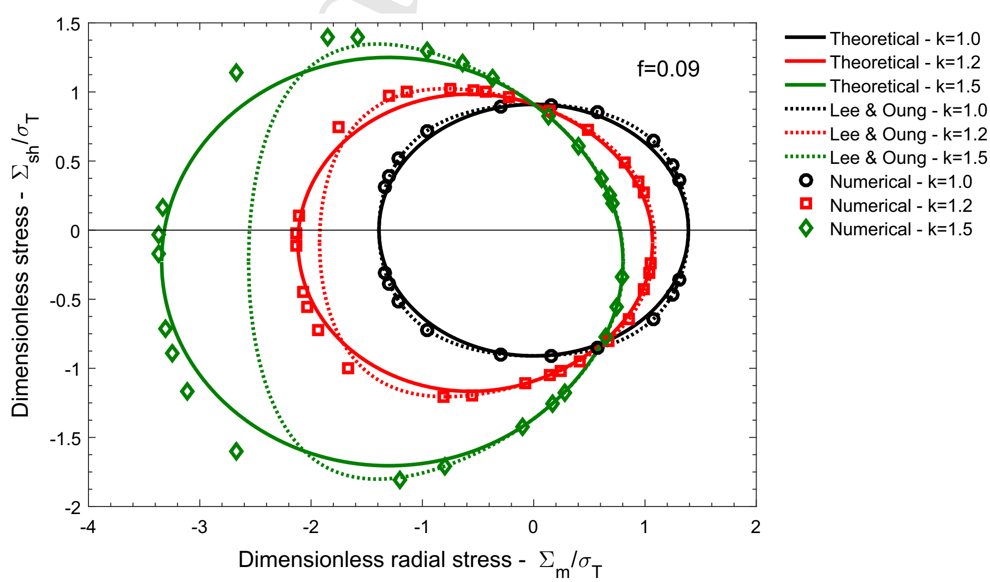

Fig. 9 Comparison between theoretical (Eq. (35)), the approximate criterion of Lee and Oung [24] (Eq. C.6) and finite element results for $f = 0.09$ and different values of parameter $k = (1.0,\ 1.2,\ 1.5)$: yield surfaces plotted in the plane of the dimensionless equivalent shear stress Σ_{sh}/σ_T *versus* the dimensionless mean lateral stress Σ_m/σ_T. Notice that, for the axisymmetric cylindrical case shown in Fig. 1c, we have $\Sigma_{sh} = \Sigma_3 - \Sigma_1$ and $\Sigma_m = \Sigma_1 = \Sigma_2$

material porosity f increases. Furthermore, specially for negative values of Σ_m, the yield criterion developed in this work (Eq. (35)) provides better predictions when compared with the approximate function proposed by Lee and Oung [24] (Eq. (C.6)). The latter strongly underestimates the effective material strength when small porosities, higher values of k and high triaxialities are considered. Those observations have already been reported by Monchiet and Kondo [30] and Shen et al. [41] in the case of a hollow sphere with Mises–Schleicher matrix material.

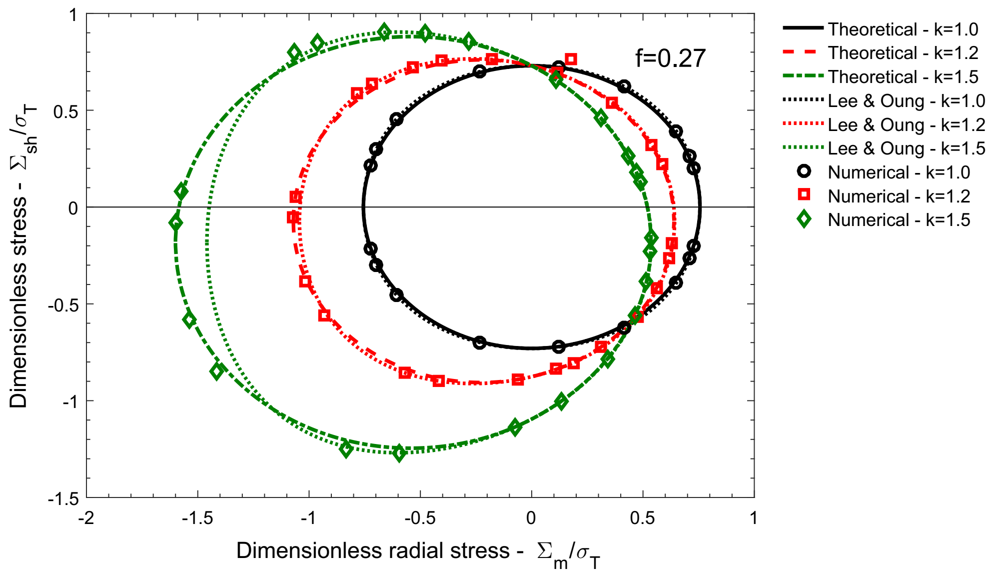

Fig. 10 Comparison between theoretical (Eq. (35)), the approximate criterion of Lee and Oung [24] (Eq. C.6) and finite element results for $f = 0.27$ and different values of parameter $k = (1.0,\ 1.2,\ 1.5)$: yield surfaces plotted in the plane of the dimensionless equivalent shear stress Σ_{sh}/σ_T *versus* the dimensionless mean lateral stress Σ_m/σ_T. Notice that, for the axisymmetric cylindrical case shown in Fig. 1c, we have $\Sigma_{sh} = \Sigma_3 - \Sigma_1$ and $\Sigma_m = \Sigma_1 = \Sigma_2$

6 Summary and concluding remarks

In this work, a closed-form yield criterion (Eq. (35)), for porous materials with pressure-dependent and tension–compression asymmetric matrix (Mises–Schleicher–Burzyński material) containing cylindrical voids, has been developed. The overall development is based on the stress-based variational homogenization approach proposed by Cheng et al. [8]. The model developed here recovers the matrix material behavior for a null porosity value. However, since a stress-based procedure has been employed, it does not recover Gurson's model when a tension–compression symmetric (von Mises) matrix is adopted. Proposed yield criterion has been assessed comparing its predictions with finite element simulations. In addition, results obtained using the model developed by Lee and Oung [24] (Eq. (C.6)) have also been considered in comparisons. The studies have taken into account different porosities, $f = (0.00,\ 0.01,\ 0.03,\ 0.09,\ 0.27)$, and distinct tension–compression asymmetries, $k = (1.0,\ 1.2,\ 1.5)$. In general, the whole analysis shows that the proposed model provides lower estimative for the yield surface when compared to the finite element results. For all values of k considered in this study, the highest differences ($\sim 31\,\%$) between the present model and numerical results have been observed when $f = 0.01$ for stress triaxiliaties (T) close to -2 and $k = 1.5$. However, while the differences are observed to increase with k, a better agreement with finite element simulations are obtained when the material porosity increases. Furthermore, specially for negative values of Σ_m, the yield criterion developed in this work gives better predictions when compared with Lee and Oung's model. The latter strongly underestimates the numerical results when small porosities, higher values of k and high triaxialities are considered. It is expected that the model proposed here can be improved as the trial stress field is enriched. In the present approach, the microscopic trial stress field has been obtained from the superposition of two exact solutions, providing: (i) a purely hydrostatic macroscopic stress state ($T = \pm\infty$); (ii) and a uniaxial macroscopic stress state in the longitudinal direction ($T = \pm 1/3$). However, if another stress solution, resulting in an intermediate value of T, can be obtained, the theoretical model could be improved and provide predictions closer to the reference results. It is expected the main finds of this work can be used to the plastic analysis of honeycomb structures or additively manufactured materials, where metal matrix composites are employed. Our theoretical development has considered a perfectly plastic material, which is not the case for real materials. However, a strain hardening rule, such as that proposed by Zhang et al. [54] to metal matrix composites, can be heuristically added to the matrix material strength. This procedure has been extensively done to Gurson's model in the literature. To be emphasized that, since phenomena such as internal necking and void coalescence (see for instance Benzerga and Leblond [2]) have not been taken into account here, the effects of such failure mechanisms also deserve to be addressed in future works. In addition, the present study could also be further extended to the dynamic analysis of porous materials following the approach of Molinari and co-authors [27, 45]. According to their rationale, the total stress tensor is given by the superposition of a static stress, obtained from a rate potential, and a dynamic stress, accounting for micro-inertia effects. Certainly, safe use of the proposed strength criterion, and its extensions, in practical engineering applications demands further validations against experiments on porous materials/structures. Therefore, to complement both numerical and theoretical results presented in this work, experimental campaigns studying the evolution of cylindrical voids in porous materials with pressure-dependent matrix presenting tension–compression asymmetry shall be conducted in future works.

Acknowledgements TdS wishes to acknowledge the financial support of FAPERGS, Fundação de Amparo à Pesquisa do Estado do Rio Grande do Sul, grant agreement 19/2551– 0001054– 0. GV want to acknowledge the financial support provided by the Spanish Ministry of Science and Innovation under Project references DPI2017-88608-P (Proyectos I+D Excelencia 2017) and EIN2019-103276 (Acciones de Dinamización Europa Investigación).

Appendix A: Development of the first stress field $\boldsymbol{\sigma}_1$

To develop the first trial stress field $\boldsymbol{\sigma}_1$, the analytical development presented by Monchiet and Kondo [30] is considered. They have proposed an exact solution for a plastic hollow sphere with a Mises–Schleicher [36] matrix material. For a plastic loading, the yield criterion has to satisfy the condition (see Eq. (3)):

$$\sigma_e^2 + 3\alpha\sigma_0\sigma_h - \sigma_0^2 = 0 \tag{A.1}$$

where, for a cylindrically symmetric problem, the von Mises equivalent stress and the hydrostatic stress are given respectively by:

$$\sigma_e = \sqrt{\frac{3}{4}(\sigma_\theta - \sigma_r)^2 + \frac{9}{4}(\sigma_z - \sigma_h)^2} \quad \text{and} \quad \sigma_h = \frac{1}{3}(\sigma_r + \sigma_\theta + \sigma_z) \tag{A.2}$$

being σ_r, σ_θ and σ_z the radial, circumferential and longitudinal stresses. For the first trial stress field $\boldsymbol{\sigma}_1$ it will be assumed that $\sigma_z = \sigma_h$, thus σ_e and σ_h become:

$$\sigma_e = \sqrt{\frac{3}{4}}(\sigma_\theta - \sigma_r)\epsilon \quad \text{and} \quad \sigma_h = \frac{1}{2}(\sigma_r + \sigma_\theta) \tag{A.3}$$

where $\epsilon = \text{sign}(\sigma_\theta - \sigma_r)$ is the sign of $(\sigma_\theta - \sigma_r)$. It is worth mentioning that, in addition to simplify the expression of the equivalent stress σ_e, assuming that $\sigma_z = \sigma_h$ results in a purely hydrostatic macroscopic stress field (see Eq. (28)).

Following the development of Monchiet and Kondo [30], a positive function $G(r)$, depending on the radial coordinate r, is introduced in a manner that:

$$\sigma_e = \sigma_0 G(r) \tag{A.4}$$

Therefore, using Eq. (A.1), the hydrostatic stress reads:

$$\sigma_h = \frac{\sigma_0}{3\alpha}\left[1 - G^2(r)\right] \tag{A.5}$$

Moreover, combining Eqs. (A.3), (A.4), (A.5), the solution in terms of σ_r and σ_θ results:

$$\sigma_r = \frac{\sigma_0}{3\alpha}\left[1 - G^2(r)\right] - \sqrt{\frac{1}{3}}\sigma_0 G(r)\epsilon \tag{A.6}$$

$$\sigma_\theta = \frac{\sigma_0}{3\alpha}\left[1 - G^2(r)\right] + \sqrt{\frac{1}{3}}\sigma_0 G(r)\epsilon \tag{A.7}$$

Introducing the last two equations into Eq. (9) yields:

$$G(r)\frac{\mathrm{d}G(r)}{\mathrm{d}r} + \frac{A}{2}\frac{dG(r)}{\mathrm{d}r} + \frac{A}{r}G(r) = 0 \tag{A.8}$$

where $A = \sqrt{3}\alpha\epsilon$. The solution of the differential equation (A.8) is:

$$G(r)=\frac{A}{2}W\left(\frac{2\exp\left(\frac{C_1}{A}\right)}{Ar^2}\right)$$

or

$$G(r)=\frac{\sqrt{3}\alpha\epsilon}{2}W\left(p\frac{a^2}{r^2}\right) \tag{A.9}$$

where $W(x)$ is the Lambert W function, which is the inverse of $x=W\exp(W)$. Function p is defined as:

$$p=\frac{2\exp\left(\frac{C_1}{\sqrt{3}\alpha\epsilon}\right)}{\sqrt{3}\alpha\epsilon a^2} \tag{A.10}$$

Thus, parameter p has both positive (p_+) and negative (p_-) branches:

$$p=\begin{cases} p_+=\frac{2\exp\left(\frac{C_1}{\sqrt{3}\alpha}\right)}{\sqrt{3}\alpha a^2} \\ p_-=-\frac{2\exp\left(-\frac{C_1}{\sqrt{3}\alpha}\right)}{\sqrt{3}\alpha a^2} \end{cases} \tag{A.11}$$

Since $G(r)\geq 0$, from Eqs. (A.9) and (A.11), it is concluded that $\mathrm{sign}(W)=\mathrm{sign}(p)$ and thus $\epsilon=\mathrm{sign}(p)$.

Given the solution (A.9), the stress components become (see Eqs. (A.6) and (A.7)):

$$\sigma_r=\frac{\sigma_0}{3\alpha}\left[1-\frac{3\alpha^2}{4}W^2\left(p\frac{a^2}{r^2}\right)-\frac{3\alpha^2}{2}W\left(p\frac{a^2}{r^2}\right)\right] \tag{A.12}$$

$$\sigma_\theta=\frac{\sigma_0}{3\alpha}\left[1-\frac{3\alpha^2}{4}W^2\left(p\frac{a^2}{r^2}\right)+\frac{3\alpha^2}{2}W\left(p\frac{a^2}{r^2}\right)\right] \tag{A.13}$$

From Eq. $(\mathrm{A.3})_2$, the hydrostatic and axial stresses are then calculated:

$$\sigma_h=\sigma_z=\frac{\sigma_0}{3\alpha}\left[1-\frac{3\alpha^2}{4}W^2\left(p\frac{a^2}{r^2}\right)\right] \tag{A.14}$$

Coefficient p can be determined from the boundary condition $\sigma_r(r=a)=0$. Thus, from Eq. (A.12):

$$\alpha^2W^2(p)+2\alpha^2W(p)-\frac{4}{3}=0 \tag{A.15}$$

The corresponding roots of the last equation are:

$$W(p)=\frac{-\alpha\pm\sqrt{\alpha^2+\frac{4}{3}}}{\alpha}$$

Thus, both the positive (p_+) and negative (p_-) branches of p are determined:

$$\begin{cases} p=p_+=z_+\exp(z_+), \quad z_+=\frac{-\alpha+\sqrt{\alpha^2+\frac{4}{3}}}{\alpha} \\ \text{or} \\ p=p_-=z_-\exp(z_-), \; z_-=\frac{-\alpha-\sqrt{\alpha^2+\frac{4}{3}}}{\alpha} \end{cases} \tag{A.16}$$

Appendix B: Development of the second stress field $\boldsymbol{\sigma}_2$

To develop the second trial stress field $\boldsymbol{\sigma}_2$, a homogeneous longitudinal stress state is considered:

$$\boldsymbol{\sigma}_2 = \sigma_z \boldsymbol{e}_z \otimes \boldsymbol{e}_z \tag{B.1}$$

Since σ_z is constant, the stress tensor $\boldsymbol{\sigma}_2$ readily satisfies the equilibrium equation div$\boldsymbol{\sigma}_2 = \mathbf{0}$. For this particular stress tensor, the von Mises equivalent stress and the hydrostatic stress become, respectively:

$$\sigma_e = \sigma_z \mathrm{sign}(\sigma_z) \quad \text{and} \quad \sigma_h = \frac{1}{3}\sigma_z \tag{B.2}$$

Therefore, the yield condition yields (see Eq. (3)):

$$\sigma_z^2 + \alpha\sigma_0\sigma_z - \sigma_0^2 = 0 \tag{B.3}$$

Thus, solving previous equation in terms of the longitudinal stress, we obtain:

$$\sigma_z = \left(-\alpha \pm \sqrt{\alpha^2+4}\right)\frac{\sigma_0}{2} \tag{B.4}$$

Since $\sigma_0 > 0$, the term $\left(-\alpha \pm \sqrt{\alpha^2+4}\right)$ defines the sign of the longitudinal stress σ_z. Notice in Eq. (B.4) that the solution depends on the tension–compression asymmetry by means of parameter α (or k, see Eq. (2)).

Appendix C: Development of the macroscopic yield function $\Phi(\boldsymbol{\Sigma})$

This section is intended to present the development leading to the macroscopic yield function $\Phi(\boldsymbol{\Sigma})$. Starting from condition (19), having in mind the matrix yield function (3), the following relation is obtained:

$$\Phi(\boldsymbol{\Sigma}) = \frac{1}{|\Omega|}\int_a^b \int_{-\frac{H}{2}}^{\frac{H}{2}} \int_0^{2\pi} \left(\sigma_e^2 + 3\alpha\sigma_0\sigma_h - \sigma_0^2\right) r d\theta \mathrm{d}z \mathrm{d}r \tag{C.1}$$

In view of the stress superposition (21) and the trial stress fields given in Eqs. (22)–(24) and (30), the first term in the right-hand side of Eq. (C.1), can be integrated as follows:

$$\begin{aligned}\frac{1}{|\Omega|}\int_{-\frac{H}{2}}^{\frac{H}{2}} \int_0^{2\pi} \int_a^b \sigma_e^2 r \mathrm{d}r \mathrm{d}\theta \mathrm{d}z &= \frac{1}{|\Omega|}\int_{-\frac{H}{2}}^{\frac{H}{2}} \int_0^{2\pi} \int_a^b \left[A_1^2 \frac{3\alpha^2}{4} W^2\left(p\frac{a^2}{r^2}\right) + \frac{9}{4}\left(\frac{2}{3}A_2\right)^2\right] r \mathrm{d}r \mathrm{d}\theta \mathrm{d}z \\ &= -\left(f + \frac{3\alpha^2}{4}\Upsilon\right)A_1^2 + A_2^2(1-f)\end{aligned} \tag{C.2}$$

in which relations $|\Omega| = H\pi b^2$, $f = \frac{a^2}{b^2}$ and condition (A.15) have been employed. Moreover, parameter Υ is calculated using in Eq. (29).

Moreover, also using Eqs. (21), (22)–(24) and (30), the second term in the right-hand side of Eq. (C.1) is integrated:

$$\begin{aligned}\frac{3\alpha\sigma_0}{|\Omega|}\int_{-\frac{H}{2}}^{\frac{H}{2}} \int_0^{2\pi} \int_a^b \sigma_h r \mathrm{d}r \mathrm{d}\theta \mathrm{d}z &= \frac{2\pi H\sigma_0 A_1}{\Omega}\int_a^b \left[1 - \frac{3\alpha^2}{4} W^2\left(p\frac{a^2}{r^2}\right)\right] r \mathrm{d}r + \frac{2\pi H\alpha\sigma_0 A_2}{\Omega}\int_a^b r dr \\ &= \sigma_0\left(1 + \frac{3}{4}\alpha^2\Upsilon\right)A_1 + (1-f)\alpha\sigma_0 A_2\end{aligned} \tag{C.3}$$

where relations $|\Omega| = H\pi b^2$, $f = \frac{a^2}{b^2}$ and Eq. (A.15) have been used again.

Finally, the last term on the right hand side of Eq. (C.1) can be easily integrated:

$$\frac{1}{|\Omega|}\int_{-\frac{H}{2}}^{\frac{H}{2}} \int_0^{2\pi} \int_a^b \sigma_0^2 r dr d\theta \mathrm{d}z = (1-f)\sigma_0^2 \tag{C.4}$$

Therefore, using Eqs. (C.2)–(C.4), Eq. (C.1) becomes:

$$\Phi(\boldsymbol{\Sigma}) = -\left(f + \frac{3\alpha^2}{4}\Upsilon\right)A_1^2 + A_2^2(1-f) + \sigma_0\left(1 + \frac{3}{4}\alpha^2\Upsilon\right)A_1 + (1-f)\alpha\sigma_0 A_2 - (1-f)\sigma_0^2 = 0 \tag{C.5}$$

Appendix D: Reference criteria to porous materials with cylindrical voids

This section aims at summarizing yield criteria that have been proposed in the literature to porous materials with cylindrical voids. Those criteria will be considered in this work for comparison purposes. The first one is the well-known [17] criterion:

$$\Phi_G = \frac{\Sigma_e^2}{\sigma_0^2} + 2f\cosh\left(\frac{\sqrt{3}\Sigma_m}{\sigma_0}\right) - \left(1+f^2\right) = 0 \tag{D.1}$$

where Σ_e is the von Mises equivalent stress and $\Sigma_m = (\Sigma_1+\Sigma_2)/2$ denotes the mean lateral stress. In the specific axisymmetric case of the cylinder shown in Fig. 1c, we have $\Sigma_m = \Sigma_1 = \Sigma_2$ and $\Sigma_e = |\Sigma_3 - \Sigma_1|$, that is, the von Mises equivalent stress has the absolute value of the equivalent shear stress Σ_{sh} defined in Eq. (32). For a purely hydrostatic loading ($\Sigma_e = \Sigma_{sh} = 0$), Eq. (D.1) provides the well-known exact solution:

$$|\Sigma_m| = \frac{\sigma_0}{\sqrt{3}}\ln(f) \tag{D.2}$$

where the identity $\operatorname{arcosh}(x) = \ln\left(x + \sqrt{x^2-1}\right)$, for $x \geq 1$, has been used. Notice that, for a purely hydrostatic case, we have $\Sigma_m = \Sigma_h$, being Σ_h the hydrostatic stress.

The second one is the upper bound that has been developed by Lee and Oung [24] employing Gurson's kinematic approach to porous materials with Mises–Schleicher matrix material:

$$\Phi_{LO}^{up} = \frac{\Sigma_{sh}^2}{\sigma_0^2} + 3f\frac{\Sigma_m^2}{\sigma_0^2} + \alpha(1-f)\frac{(3\Sigma_m + \Sigma_{sh})}{\sigma_0} - (1-f)^2 = 0 \tag{D.3}$$

where relation $\Sigma_e = \pm\Sigma_{sh}$, between the equivalent von Mises stress Σ_e and the equivalent shear stress Σ_{sh} (See Eq. (32)), has been employed in order to have the same stress components shown in Eq. (35). For a purely hydrostatic stress state ($\Sigma_{sh} = 0$), previous criterion becomes:

$$3f\frac{\Sigma_m^2}{\sigma_0^2} + 3\alpha(1-f)\frac{\Sigma_m}{\sigma_0} - (1-f)^2 = 0 \tag{D.4}$$

In addition, when the special case with $\alpha \to 0$ is considered, it results:

$$|\Sigma_m| = \frac{\sigma_0}{\sqrt{3}}\frac{(1-f)}{\sqrt{f}} \tag{D.5}$$

which differs from the exact solution (D.2). In order to recover Gurson's model when $\alpha \to 0$ (von Mises matrix material) and also to provide better predictions for high triaxialities, the previous criterion (Eq. (D.3)) has been heuristically modified by Lee and Oung [24]. Their improved approximate criterion reads:

$$\Phi_{LO}^{app} = \frac{\Sigma_{sh}^2}{\sigma_0^2} + 2f\cosh\left(\frac{\sqrt{3}\Sigma_m}{\sigma_0}\right) + \alpha(1-f)\frac{(3\Sigma_m + \Sigma_{sh})}{\sigma_0} - \left(1+f^2\right) = 0 \tag{D.6}$$

where relation $\Sigma_e = \pm\Sigma_{sh}$ has been used. Considering a purely hydrostatic loading ($\Sigma_{sh} = 0$), the improved criterion yields:

$$2f\cosh\left(\frac{\sqrt{3}\Sigma_m}{\sigma_0}\right) + 3\alpha(1-f)\frac{\Sigma_m}{\sigma_0} - \left(1+f^2\right) = 0 \tag{D.7}$$

which clearly recovers Eq. (D.2) when $\alpha \to 0$.

References

1. ABAQUS/Standard: Simulia, User's Manual. Dassault Systémes, Providence, USA. version 6.19 edition (2019)
2. Benzerga, A.A., Leblond, J.B.: Ductile fracture by void growth to coalescence. In: Aref, H., van der Giessen, E. (eds.) Advances in Applied Mechanics. Advances in Applied Mechanics, vol. 44, pp. 169–305. Elsevier, Amsterdam (2010)
3. Burzyński, W.: Ueber die anstrengungshypothesen. Schweiz Bauzeitung **94**, 259–262 (1929)
4. Castañeda, P.P.: Nonlinear Composite Materials: Effective Constitutive Behavior and Microstructure Evolution, pp. 131–195. Springer, Vienna (1997)
5. Cazacu, O., Plunkett, B., Barlat, F.: Orthotropic yield criterion for hexagonal closed packed metals. Int. J. Plast. **22**, 1171–1194 (2006)
6. Cazacu, O., Stewart, J.B.: Analytic plastic potential for porous aggregates with matrix exhibiting tension-compression asymmetry. J. Mech. Phys. Solids **57**, 325–341 (2009)
7. Cheng, L., Guo, T.: Void interaction and coalescence in polymeric materials. Int. J. Solids Struct. **44**, 1787–1808 (2007)
8. Cheng, L., de Saxcé, G., Kondo, D.: A stress-based variational model for ductile porous materials. Int. J. Plast. **55**, 133–151 (2014)
9. Coussy, O.: Poromechanics. Wiley, Hoboken (2004)
10. Coussy, O.: Mechanics and Physics of Porous Solids. Wiley, Hoboken (2011)
11. Dormieux, L., Lemarchand, E., Kondo, D., Brach, S.: Strength criterion of porous media: application of homogenization techniques. J. Rock Mech. Geotech. Eng. **9**, 62–73 (2017)
12. Durban, D., Cohen, T., Hollander, Y.: Plastic response of porous solids with pressure sensitive matrix. Mech. Res. Commun. **37**, 636–641 (2010)
13. Eve, R.A., Reddy, B.D., Rockafellar, R.T.: An internal variable theory of elastoplasticity based on the maximum plastic work inequality. Q. Appl. Math. **48**, 59–83 (1990)
14. Fritzen, F., Forest, S., Kondo, D., Böhlke, T.: Computational homogenization of porous materials of green type. Comput. Mech. **52**, 121–134 (2013)
15. Gologanu, M., Leblond, J.B., Devaux, J.: Approximate models for ductile metals containing non-spherical voids-case of axisymmetric prolate ellipsoidal cavities. J. Mech. Phys. Solids **41**, 1723–1754 (1993)
16. Guo, T., Faleskog, J., Shih, C.: Continuum modeling of a porous solid with pressure-sensitive dilatant matrix. J. Mech. Phys. Solids **56**, 2188–2212 (2008)
17. Gurson, A.: Continuum theory of ductile rupture by void nucleation and growth. Part I: yield criteria and flow rules for porous ductile media. ASME J. Eng. Mater. Technol. **99**, 2–15 (1977)
18. Halphen, B., Son Nguyen, Q.: Sur les matériaux standard généralisés. J. de Mécanique **14**, 39–63 (1975)
19. Han, B., Shen, W., Xie, S., Shao, J.: Plastic modeling of porous rocks in drained and undrained conditions. Comput. Geotech. **117**, 103277 (2020)
20. Hill, R.: A theory of the yielding and plastic flow of anisotropic metals. Proc. R. Soc. Lond. Ser. A Math. Phys. Sci. **193**, 281–297 (1948)
21. Keralavarma, S., Benzerga, A.: A constitutive model for plastically anisotropic solids with non-spherical voids. J. Mech. Phys. Solids **58**, 874–901 (2010)
22. Keralavarma, S., Benzerga, A.: Numerical assessment of an anisotropic porous metal plasticity model. Mechanics of Materials 90, 212–228. Proceedings of the IUTAM Symposium on Micromechanics of Defects in Solids (2015)
23. Leblond, J., Perrin, G., Suquet, P.: Exact results and approximate models for porous viscoplastic solids. Int. J. Plast. **10**, 213–235 (1994)
24. Lee, J., Oung, J.: Yield functions and flow rules for porous pressure-dependent strain-hardening polymeric materials. J. Appl. Mech. **67**, 288–297 (2000)
25. Martin, J.H., Yahata, B.D., Clough, E.C., Mayer, J.A., Hundley, J.M., Schaedler, T.A.: Additive manufacturing of metal matrix composites via nanofunctionalization. MRS Commun. **8**, 297–302 (2018)
26. McClintock, F.A.: A criterion for ductile fracture by the growth of holes. J. Appl. Mech. **35**, 363–371 (1968)
27. Molinari, A., Mercier, S.: Micromechanical modelling of porous materials under dynamic loading. J. Mech. Phys. Solids **49**, 1497–1516 (2001)
28. Monchiet, V., Cazacu, O., Charkaluk, E., Kondo, D.: Macroscopic yield criteria for plastic anisotropic materials containing spheroidal voids. Int. J. Plast. **24**, 1158–1189 (2008)
29. Monchiet, V., Charkaluk, E., Kondo, D.: Macroscopic yield criteria for ductile materials containing spheroidal voids: an eshelby-like velocity fields approach. Mech. Mater. **72**, 1–18 (2014)
30. Monchiet, V., Kondo, D.: Exact solution of a plastic hollow sphere with a Mises–Schleicher matrix. Int. J. Eng. Sci. **51**, 168–178 (2012)
31. Moreau, J.: Application of convex analysis to the treatment of elastoplastic systems, in: Germain, P., Nayroles, B. (Eds.), Applications of Methods of Functional Analysis to Problems in Mechanics. Springer Berlin / Heidelberg. volume 503 of *Lecture Notes in Mathematics*, pp. 56–89. https://doi.org/10.1007/BFb0088746 (1976)
32. Pastor, F., Anoukou, K., Pastor, J., Kondo, D.: Limit analysis and homogenization of porous materials with Mohr-coulomb matrix. part ii: Numerical bounds and assessment of the theoretical model. J. Mech. Phys. Solids **91**, 14–27 (2016)
33. Pastor, F., Kondo, D., Pastor, J.: 3d-fem formulations of limit analysis methods for porous pressure-sensitive materials. Int. J. Numer. Methods Eng. **95**, 847–870 (2013)
34. Pastor, F., Kondo, D., Pastor, J.: Limit analysis and computational modeling of the hollow sphere model with a Mises–Schleicher matrix. Int. J. Eng. Sci. **66–67**, 60–73 (2013)
35. Rice, J., Tracey, D.: On the ductile enlargement of voids in triaxial stress fields. J. Mech. Phys. Solids **17**, 201–217 (1969)
36. Schleicher, F.: Der spannungszustand an der fließgrenze (plastizitätsbedingung). ZAMM J. Appl. Math. Mech. Z. für Angew. Math. und Mech. **6**, 199–216 (1926). https://doi.org/10.1002/zamm.19260060303
37. Shen, W., Oueslati, A., de Saxcé, G.: Macroscopic criterion for ductile porous materials based on a statically admissible microscopic stress field. Int. J. Plast. **70**, 60–76 (2015)

38. Shen, W., Shao, J.: Some micromechanical models of elastoplastic behaviors of porous geomaterials. J. Rock Mech. Geotech. Eng. **9**, 1–17 (2017)
39. Shen, W., Shao, J.: A micro-mechanics-based elastic-plastic model for porous rocks: applications to sandstone and chalk. Acta Geotech. **13**, 329–340 (2018)
40. Shen, W., Shao, J., Dormieux, L., Kondo, D.: Approximate criteria for ductile porous materials having a green type matrix: application to double porous media. Comput. Mater. Sci. **62**, 189–194 (2012)
41. Shen, W., Shao, J., Kondo, D., Saxcé, G.D.: A new macroscopic criterion of porous materials with a Mises–Schleicher compressible matrix. Eur. J. Mech. A/Solids **49**, 531–538 (2015)
42. Shen, W., Shao, J., Liu, Z.: Evaluation and improvement of macroscopic yield criteria of porous media having a drucker-prager matrix. Int. J. Plast. (2019)
43. Shen, W., Shao, J., Oueslati, A., Saxcé, G.D., Zhang, J.: An approximate strength criterion of porous materials with a pressure sensitive and tension-compression asymmetry matrix. Int. J. Eng. Sci. **132**, 1–15 (2018)
44. Shen, W., Zhang, J., Shao, J., Kondo, D.: Approximate macroscopic yield criteria for drucker-prager type solids with spheroidal voids. Int. J. Plast. **99**, 221–247 (2017)
45. Subramani, M., Czarnota, C., Mercier, S., Molinari, A.: Dynamic response of ductile materials containing cylindrical voids. Int. J. Fract. 1–22 (2020)
46. Suquet, P.: Effective Properties of Nonlinear Composites, pp. 197–264. Springer, Vienna (1997)
47. Suquet, P.M.: Elements of homogenization for inelastic solid mechanics, homogenization techniques for composite media. Lect. Notes Phys. **272**, 193 (1985)
48. Trillat, M., Pastor, J.: Limit analysis and Gurson's model. Eur. J. Mech. A/Solids **24**, 800–819 (2005)
49. Tvergaard, V.: Influence of voids on shear band instabilities under plane strain conditions. Int. J. Fract. **17**, 389–407 (1981)
50. Tvergaard, V., Needleman, A.: Analysis of the cup-cone fracture in a round tensile bar. Acta Metall. **32**, 157–169 (1984)
51. Vadillo, G., Fernández-Sáez, J.: An analysis of Gurson model with parameters dependent on triaxiality based on unitary cells. Eur. J. Mech. A/Solids **28**, 417–427 (2009)
52. Vadillo, G., Fernández-Sáez, J., Pęcherski, R.: Some applications of Burzyński yield condition in metal plasticity. Mater. Des. **32**, 628–635 (2011)
53. Yi, S., Duo, W.: A lower bound approach to the yield loci of porous materials. Acta Mech. Sin. **5**, 237–243 (1989)
54. Zhang, H., Ramesh, K., Chin, E.: A multi-axial constitutive model for metal matrix composites. J. Mech. Phys. Solids **56**, 2972–2983 (2008)
55. Zhang, J., Shen, W., Oueslati, A., Saxcé, G.D.: Shakedown of porous materials. Int. J. Plast. **95**, 123–141 (2017)

Journal: 707
Article:

Author Query Form

Please ensure you fill out your response to the queries raised below and return this form along with your corrections

Dear Author

During the process of typesetting your article, the following queries have arisen. Please check your typeset proof carefully against the queries listed below and mark the necessary changes either directly on the proof/online grid or in the 'Author's response' area provided below

Query	Details required	Author's response
1.	Kindly provide complete details for the references [42, 45].	